IOP Publishing Reports on Progress in Physics
Rep. Prog. Phys. 79 (2016) 064503 (20pp) doi:10.1088/0034-4885/79/6/064503

Report on Progress

Non-equilibrium control of complex solids by nonlinear phononics

Roman Mankowsky[1], Michael Först[1] and Andrea Cavalleri[1,2]

[1] Max Planck Institute for the Structure and Dynamics of Matter, 22761 Hamburg, Germany
[2] Department of Physics, Clarendon Laboratory, Oxford University, Oxford, OX1 3PU, UK

E-mail: andrea.cavalleri@mpsd.mpg.de

Invited by Laura Greene

Received 26 October 2015, revised 7 March 2016
Accepted for publication 10 March 2016
Published 23 May 2016

Abstract

We review some recent advances in the use of optical fields at terahertz frequencies to drive the lattice of complex materials. We will focus on the control of low energy collective properties of solids, which emerge *on average* when a high frequency vibration is driven and a new crystal structure induced. We first discuss the fundamentals of these lattice rearrangements, based on how anharmonic mode coupling transforms an oscillatory motion into a quasi-static deformation of the crystal structure. We then discuss experiments, in which selectively changing a bond angle turns an insulator into a metal, accompanied by changes in charge, orbital and magnetic order. We then address the case of light induced non-equilibrium superconductivity, a mysterious phenomenon observed in some cuprates and molecular materials when certain lattice vibrations are driven. Finally, we show that the dynamics of electronic and magnetic phase transitions in complex-oxide heterostructures follow distinctly new physical pathways in case of the resonant excitation of a substrate vibrational mode.

Keywords: nonlinear phononics, correlated electron systems, light-induced phase transitions

(Some figures may appear in colour only in the online journal)

1. Introduction to nonlinear lattice control

Terahertz (THz) frequency optical fields at strengths in excess of 100 kV cm^{-1} can be used to resonantly excite collective modes in solids, provided that these modes are at long wavelengths ($q \sim 0$) and infrared-active, that is, changes in their coordinate Q involve a change in dipole moment. Lattice vibrations can selectively be driven to amplitudes as high as several percent of interatomic distances. A situation, in which all modes are at low temperatures whereas one is populated coherently to such large amplitude, is new and highly unusual. Crucially, dynamical states are created that may have radically different *average* properties than the same materials at equilibrium.

The linear response of a crystal lattice to a light field made resonant with an infrared-active phonon mode is described by the potential energy term $V_{\mathrm{lin}} = \frac{1}{2}\,\omega_{\mathrm{IR}}^2 Q_{\mathrm{IR}}^2$. In this expression, Q_{IR} is the normal coordinate of the mode and ω_{IR} its eigenfrequency. When resonantly driven by a pulsed field of the type $f(t) = F(t)\sin(\omega_{\mathrm{IR}}t)$, for which $F(t)$ is a Gaussian envelope function, the dynamics can be described by the equation of motion of a damped harmonic oscillator

$$\ddot{Q}_{\mathrm{IR}} + 2\gamma_{\mathrm{IR}}\dot{Q}_{\mathrm{IR}} + \omega_{\mathrm{IR}}^2 Q_{\mathrm{IR}} = f(t), \qquad (1)$$

where γ_{IR} is damping constant of the mode. Following the excitation, the atoms oscillate about their equilibrium positions along the normal coordinate of the mode and relax over a timescale determined by the duration of the envelope function or by the decay time $1/\gamma_{\mathrm{IR}}$, whichever is longer.

By increasing the strength of the driving electric field, anharmonic coupling to other modes with generic coordinate

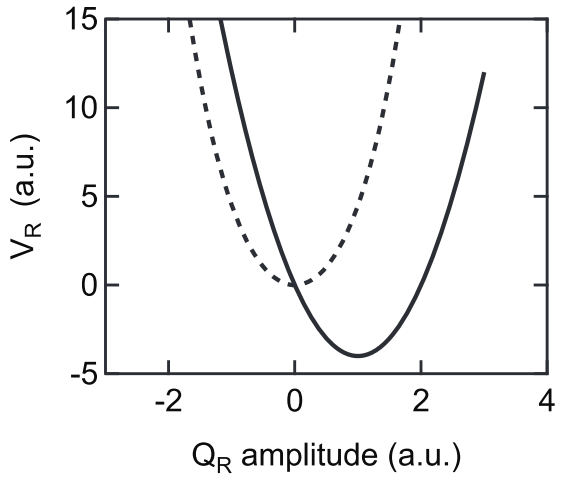

Figure 1. Parabolic energy potential V_R of a Raman-active phonon mode (dashed curve). Within cubic coupling, this energy potential shifts towards a new position (solid curve) for a finite static displacement of a coupled infrared-active mode Q_{IR}.

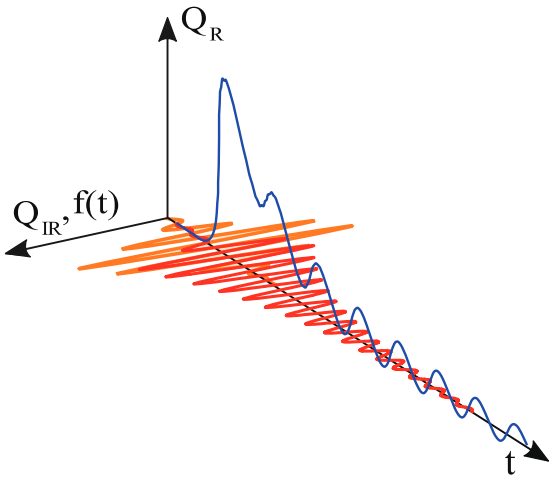

Figure 2. The dynamical response of the two coupled modes within cubic coupling. Following excitation by the electric field $f(t)$ (orange), the infrared-active mode Q_{IR} (red) starts to oscillate coherently about the equilibrium position, while Q_R (blue) undergoes a directional displacement, which scales with Q_{IR}^2. This displacement survives as long as the Q_{IR} amplitude is finite. If the optical excitation is short compared to the Raman phonon period, coherent oscillations along Q_R take place, which decay with the dephasing time of the Raman mode.

Q_R becomes important. In the limit of cubic coupling, the lattice potential describing the nonlinear interaction reads

$$V_{NL} = \frac{1}{2}\omega_R^2 Q_R^2 - a_{12} Q_{IR} Q_R^2 - a_{21} Q_{IR}^2 Q_R, \qquad (2)$$

where a_{ij} are anharmonic coupling constants. Equation (2) is simplified if we consider only centrosymmetric crystals, for which infrared-active phonon modes are of odd parity while Raman-active modes are even. For symmetry reasons, the first coupling term $a_{12} Q_{IR} Q_R^2$ is always zero and the second term $a_{21} Q_{IR}^2 Q_R$ is nonzero only if Q_R is a Raman mode. For a finite static displacement Q_{IR}^* of the infrared-active mode, this nonlinear phonon interaction induces a shift of the Raman mode's energy potential V_R along its coordinate Q_R, as depicted in figure 1. These physics were analyzed theoretically in the 1970s, casted in the framework of Ionic Raman scattering [1–3].

For pulsed excitation of the infrared-active mode Q_{IR}, the coupled dynamics are described by the two equations of motion, which take the form

$$\ddot{Q}_{IR} + 2\gamma_{IR}\dot{Q}_{IR} + \omega_{IR}^2 Q_{IR} = 2a_{21} Q_{IR} Q_R + f(t), \qquad (3)$$

$$\ddot{Q}_R + 2\gamma_R \dot{Q}_R + \omega_R^2 Q_R = a_{21} Q_{IR}^2. \qquad (4)$$

Key to the dynamics of the anharmonically coupled Raman mode Q_R is the driving force $a_{21} Q_{IR}^2$, with its direction being independent of the sign of Q_{IR}. Hence, the atoms of the crystal lattice not only oscillate along the infrared coordinate Q_{IR}, but are simultaneously displaced along the Raman coordinate Q_R (see figure 2). This effect is the equivalent of rectification in nonlinear optics. Furthermore, if the optical excitation is short compared to the period of the Raman mode, Q_R exhibits coherent oscillations around the quasi-static displacement amplitude.

These two effects, a displacement and oscillations are also characteristic of the well known coherent response of crystal lattices to pulsed excitation in the near-IR or visible [4–6]. However, in that case the lattice displacement and oscillations are driven by electron–phonon coupling and not, as it is the case for nonlinear phononics, by lattice anharmonicities. Note also that the excitation through nonlinear phononics is more selective and dissipation far reduced. Furthermore, the lattice displacement persists as long as the infrared mode oscillates and can thus potentially be controlled by using pulse trains or varying the duration of the excitation pulses.

2. Driving phase dynamics in magnetoresistive manganites

2.1. Nonlinear lattice dynamics

This experimental chapter starts off by introducing the first experimental observations of nonlinear phononics in the rhombohedrally-distorted perovskite $La_{0.7}Sr_{0.3}MnO_3$, a double-exchange ferromagnet with low electrical conductivity below T_c ~350 K. The infrared-active phonon mode, which was resonantly excited by mid-infrared few-cycle pump pulses to large amplitudes, comprises Mn–O stretching motions at a frequency of ~18 THz (75 meV) and is of E_u symmetry [7].

Figure 3(a) displays the time dependent anisotropic optical reflectivity changes that follow the excitation of this mode, measured in a pump-probe setup utilizing mid-infrared (14.3 μm wavelength) pump—near-infrared (800 nm wavelength) probe pulses [8]. Strikingly, the ultrafast optical response exhibits reflectivity oscillations at 1.2 THz, which—because of their frequency and their the anisotropic response—can be attributed to coherent oscillations of a Raman mode of E_g symmetry that involves the rotation of oxygen octahedra around the Mn cations [9, 10]. In addition, the pump photon energy dependent amplitude of the coherent E_g Raman mode oscillations follows the resonance profile of the infrared-active Mn–O stretching vibration, as shown in figure 3(b).

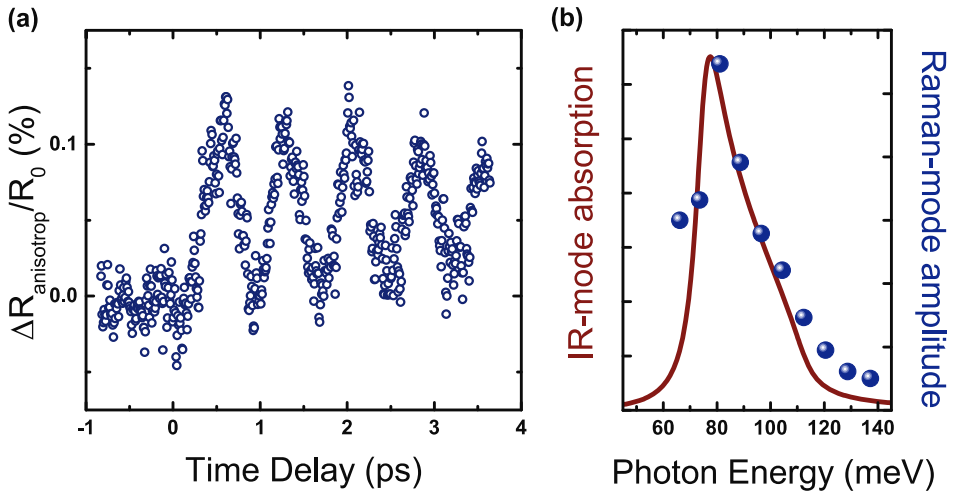

Figure 3. (a) Time-resolved anisotropic reflectivity changes in $La_{0.7}Sr_{0.3}MnO_3$ induced by the resonant excitation of the infrared-active E_u-symmetry Mn–O stretching mode at 14.3 μm wavelength (87 meV photon energy). The excitation fluence is 2 mJ cm^{-2}. Adapted from [11]. Copyright 2013 with permission from Elsevier. (b) Amplitude of the coherent E_g-symmetry Raman phonon as function of the pump photon energy. Adapted from [8]. Copyright 2011 with permission from Nature Publishing Group.

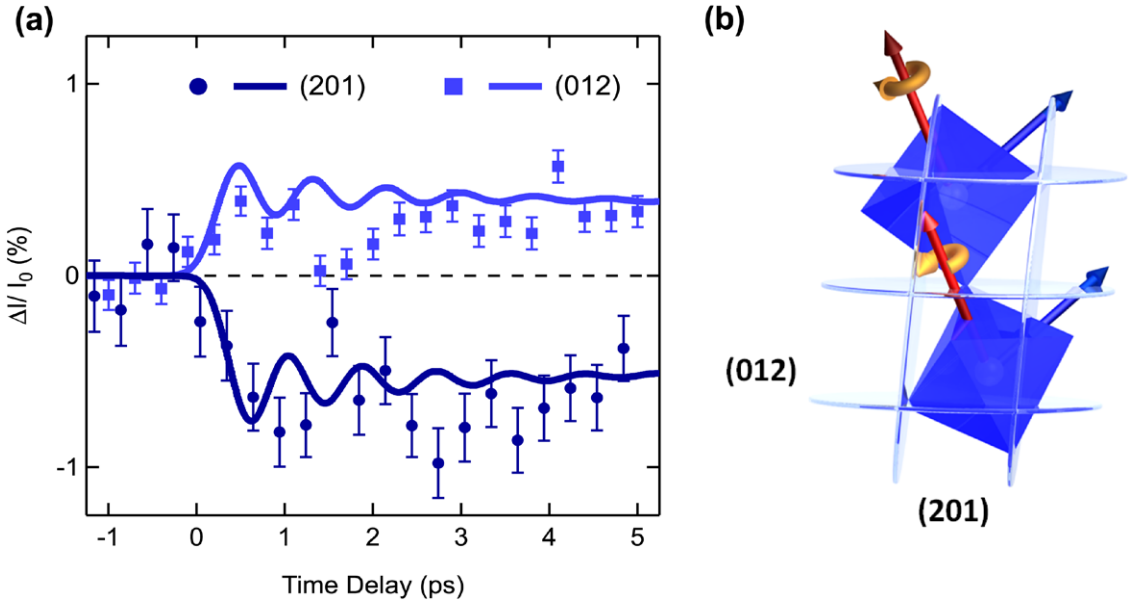

Figure 4. (a) Relative x-ray intensity changes of the (2 0 1) and the (0 1 2) Bragg peaks in $La_{0.7}Sr_{0.3}MnO_3$, induced by the same mid-infrared excitation used for the optical probe experiments above. The chosen lattice peaks are sensitive to the rotational motions of the MnO_6 octahedra associated with the E_g-symmetry Raman mode (see also illustration in panel (b)). The solid lines are the fitted intensity changes considering the coupled equations of motions for nonlinear phononics and the E_g-phonon induced structure factor changes. The anharmonic coupling constant is the only fitting parameter. Adapted from [11]. Copyright 2013 with permission from Elsevier.

These measurements clearly identified the frequency and the symmetry of the coherently driven Raman mode. However, the displacive character of the nonlinear phonon coupling could not be directly proven by this all-optical experiment.

Therefore, the modification of the crystal lattice was subsequently studied with ultrafast x-ray diffraction [11]. Atomic motions along phonon coordinates modulate the x-ray structure factor, which is reflected as characteristic changes in intensity of certain Bragg peaks [12, 13]. Thus, a study was set out to validate the predicted displacive response by measuring the intensity changes of selected Bragg peaks by time-resolved hard x-ray diffraction with femtosecond time resolution. Motions of the rotational E_g Raman mode comprise anti-phase rotations of the two MnO_6 octahedra of the $La_{0.7}Sr_{0.3}MnO_3$ unit cell [9, 10], as illustrated in figure 4(b). As only changes in the position of the oxygen atoms are involved, diffraction was measured from the {2 0 1} family of reflections, forbidden in the Mn and La/Sr sublattices of rhombohedral $La_{0.7}Sr_{0.3}MnO_3$. Due to the weak scattering from these light atoms, however, the experiment required both high x-ray flux in combination

with femtosecond time resolution, two properties uniquely provided by x-ray free electron lasers.

Figure 4(a) summarizes the results of the femtosecond x-ray diffraction experiment carried out at the linac coherent light source (LCLS) [14]. The transient intensity changes of the (2 0 1) and (0 1 2) structural Bragg peaks upon the vibrational excitation were measured with 70 fs x-ray pulses at 6 keV photon energy.

Two displacive responses were observed in the transient Bragg intensities, with different amplitudes and opposite signs for the two measured peaks. These curves were fitted by a numerical solution of the coupled equations of motion (2) and (3), further taking into account the calculated relative intensity changes $(\Delta I/I_0)/Q_R$ for a motion of the oxygen atoms with amplitude Q_R along the coordinate of the rotational Raman mode. The anharmonic coupling constant a_{21} was the only parameter that has been chosen to best fit these calculations to the experiment. Clearly, these fits indicate that the correct sign and ratio of the two structure factor changes are measured and reveal a rotation of the MnO_6 octahedra of 0.035° for the chosen excitation fluence of 1.2 mJ cm^{-2}.

2.2. Driving insulator-metal transitions

The observed conversion of the resonantly driven Mn–O stretching oscillations in $La_{0.7}Sr_{0.3}MnO_3$ into the rotation of the MnO_6 oxygen octahedra, which are strongly coupled to the collective electronic and magnetic properties, opens intriguing possibilities for the phase control of manganites. Rotations of the MnO_6 octahedra modify the Mn–O–Mn bond angles, which changes the degree of spatial overlap of the orbital wavefunctions along these bonds and controls the sign of the exchange interactions [15, 16]. In particular, the probability of 3*d* electrons for hopping between adjacent Mn sites is maximum for a bond angle of 180° (cubic lattice) and decreases with decreasing angle, resulting in maximum electron bandwidth for straight bonds. The magnetic and structural properties of manganites can be understood in more detail by considering the Goodenough–Kanamori (GK) rules for semi-covalent bonds [17], which explain the exchange interactions between neighboring manganese cations (Mn^{3+} or Mn^{4+}) connected by an oxygen anion (O^{2-}). For doped manganites, both ferromagnetic metallic or antiferromagnetic insulating behavior is possible. For asymmetric Mn^{3+}–O^{2-}–Mn^{4+} bonds, hopping occurs and the magnetic coupling is ferromagnetic as long as the bond is 'straight'. A 'bent' bond, with an angle □ 180° corresponds to an insulating, antiferromagnetic phase.

Due to this interplay, the orthorhombic manganite $Pr_{0.7}Ca_{0.3}MnO_3$ is an insulator because of its strongly distorted perovskite structure. However, these properties are unstable against various forms of external perturbation, including electric or magnetic fields and light [18–22]. Importantly, a metallic phase can also be induced by application of static pressure [23], which qualitatively can be understood as 'straightening' of the bonds.

The dynamical lattice control of the electronic phase state of a manganite was first reported by Rini *et al* [24], who measured the electric transport properties in a $Pr_{0.7}Ca_{0.3}MnO_3$ single crystal after resonant excitation of the Mn–O stretching mode. Excitation of the sample with ~1 mJ cm^{-2} femtosecond pulses at ~17 μm wavelength induced transient changes in electric transport, as shown in figure 5(a). The transition from the insulating ground state into the metastable metallic state is evident from the five-order-of-magnitude increase in electrical conductivity within the first 5 nanoseconds. Importantly, as with the nonlinear phonon response in $La_{0.7}Sr_{0.3}MnO_3$ discussed above, the strength of the insulator-metal transition in $Pr_{0.7}Ca_{0.3}MnO_3$ clearly peaks at the resonance of the Mn–O stretching mode (see figure 5(b)). Hence, the light-driven phase transition is not related to the injection of charge carriers and can be uniquely attributed to large-amplitude crystal lattice distortions.

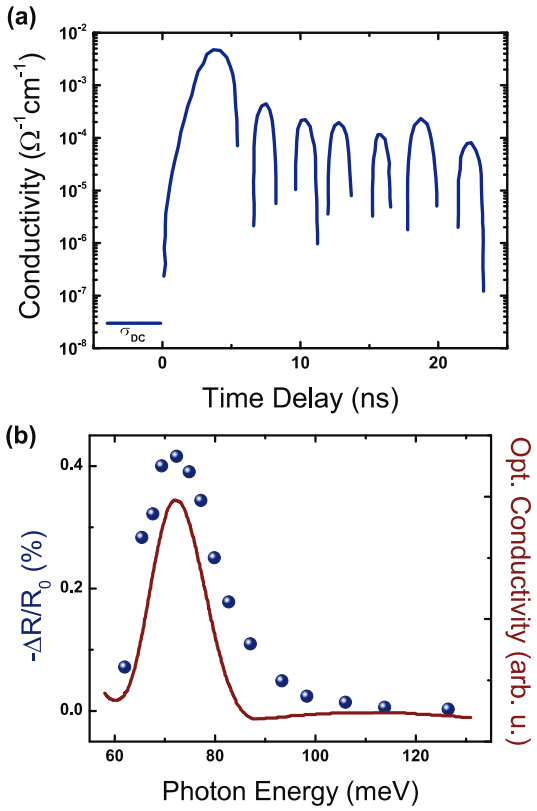

Figure 5. (a) Time-dependent electric conductivity of a $Pr_{0.7}Ca_{0.3}MnO_3$ single crystal, measured by direct current transport with a fast oscilloscope, following resonant excitation of the Mn–O stretching vibration in the mid-infrared. The DC conductivity is drastically increased as result of the vibrationally driven insulator-to-metal transition. The time resolution of this experiment was 4 ns, and the ringing at later time delays results from the fast conductivity changes and the resulting lack of impedance matching with the oscilloscope. (b) Dependence of the strength of the insulator-metal transition as function of the mid-infrared photon energy, compared with the $Pr_{0.7}Ca_{0.3}MnO_3$ optical conductivity (that is convolved with the spectral width of the excitation pulses). Adapted from [24]. Copyright 2007 with permission from Nature Publishing Group.

This conclusion was recently substantiated by a microscopic theory for the vibrationally driven ultrafast phase control, which predicts the dynamical path taken by the crystal lattice and its effect on the electronic material properties. Subedi *et al* [25] used density functional theory to compute the coupling strength of the resonantly driven Mn–O

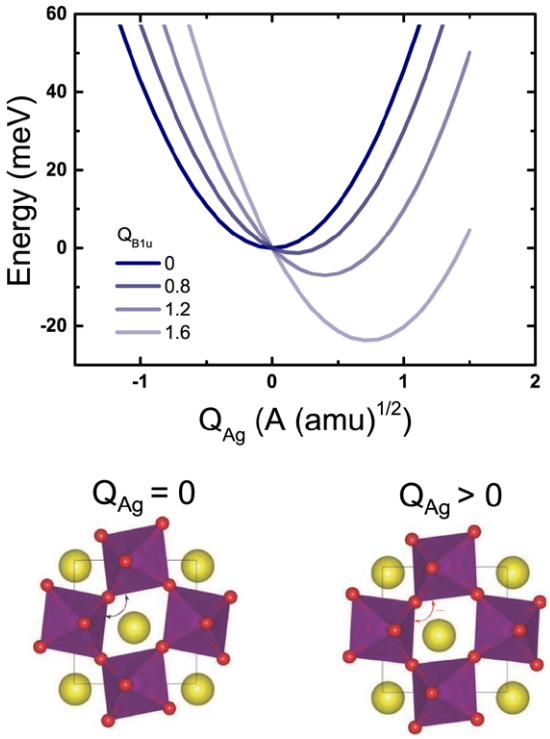

Figure 6. Calculated energy potential of the A_g in-plane rotational Raman mode in $PrMnO_3$ for different static displacements of the infrared-active B_{1u} mode. The bottom panel sketches atomic positions of the orthorhombically distorted perovskite at equilibrium (left) and for finite positive amplitude Q_{Ag} of the in-plane rotational Raman mode (right). Figure adapted from [25].

stretching mode to other phonon modes in the parent compound $PrMnO_3$. The energy potential of the strongly coupled A_g symmetry Raman mode for various amplitudes Q_{B1u} of the infrared-active B_{1u} symmetry Mn–O stretching mode is shown in figure 6(a). Finite displacement of the crystal lattice along the B_{1u} coordinate shifts the parabolic potential of a certain A_g mode to a new minimum position. As expected for the cubic $Q^2_{B1u}Q_{Ag}$ phonon coupling, the displacement of this Raman mode from the equilibrium increases quadratically with the amplitude of the infrared mode. As shown in lower panel of figure 6, the atomic motions associated with the positive amplitude of this A_g Raman mode reduce the rotation of the MnO_6 octahedra in the *ab*-plane, hence bringing the crystal structure closer to the cubic perovskite and straightening the Mn–O–Mn bonds.

According to nonlinear phononics, the excitation of the B_{1u} mode by an intense mid-infrared pulse will transiently displace the crystal lattice along these coordinates. In order to show that these motions are responsible for driving the insulator-to-metal-transitions, the electronic density of states of the manganese *3d* orbitals in this compound were also calculated by dynamical mean field theory [25]. For the equilibrium crystal structure, these calculations yield a gap at the Fermi energy, characteristic of the insulating state, which closes in the transiently displaced state. This metallization supports the hypothesis that the nonlinear coupling of the resonantly driven Mn–O stretching mode to the rotational Raman mode drives the experimentally observed insulator-metal transition in $Pr_{0.7}Ca_{0.3}MnO_3$ [24].

2.3. Melting electronic and magnetic order

The vibrationally driven ultrafast insulator-metal transition is expected to involve concomitant melting of the electronic and magnetic order present in these compounds. The first set of experiments investigating these microscopic dynamics was carried out in single-layered, half-doped $La_{0.5}Sr_{1.5}MnO_4$.

At equilibrium and below the Neél and charge/orbital ordering temperatures ($T_N = 110$ K, $T_{CO/OO} = 220$ K), this prototypical manganite exhibits complex CE-type charge, spin and orbital order. Within the *ab* planes (schematically shown in figure 7(a)), the occupied manganese *3d* e_g–like orbitals align along ferromagnetic 'zig-zag' chains, which are antiferromagnetically coupled with one another in and out of plane [26–28]. This low temperature orbital configuration breaks the tetragonal lattice symmetry, leading to a rectangular shape of the charge- and orbital-order unit cell and inducing optical birefringence [29]. More directly, resonant soft x-ray diffraction at the (¼ ¼ ½) and (¼ ¼ 0) wave vectors at the Mn $L_{2,3}$ edges, involving $2p \rightarrow 3d$ optical dipole transitions, is sensitive to this spin and charge/orbital order, providing both momentum-dependent and spectroscopic information [30–33].

Tobey *et al* [34] investigated the optical response of $La_{0.5}Sr_{1.5}MnO_4$ to the vibrationally driven phase transition. Large amplitude, coherent distortions of the Mn–O bonds were driven with femtosecond pulses at 16 μm (625 cm^{-1}, 77 meV) wavelength, resonant with a similar IR-active stretching vibration as the one studied in the cubic $Pr_{0.7}Ca_{0.3}MnO_3$. Probe pulses tunable between 10 μm (0.12 eV photon energy) and 600 nm (2.2 eV), were generated in an optical parametric amplifier.

The time-dependent reflectivity at 650 nm, measured at 90 K, below the orbital ordering temperature, is plotted in figure 7(b) showing the prompt transition into a long-lived state that survives for hundreds of picoseconds. Similar temporal profiles were detected at other wavelengths in the infrared wavelength range. The spectrally resolved reflectivity changes, detected at +100 ps time delay (see figure 7(c)), showed an increase in reflectivity at all measured photon energies below 1 eV. This transient response was compared to the measured changes in reflectivity due to an increase in temperature above the charge/orbital ordering temperature $\Delta R/R_0(\text{thermal}) = (R(300) - R(90\,K))/R(90\,K)$. The high level of agreement suggests a similarity between the photo-induced phase and the equilibrium non-ordered state. The observed increase in spectral weight below 1 eV results from the loss of a 1.3 eV inter-site charge transfer resonance in the metastable state, which at equilibrium reflects the cooperative, long-range Jahn–Teller distortion associated with the orbital ordering [35].

In addition, the ultrafast loss of orbital ordering was confirmed by measuring the time-dependent birefringence [36]. Figure 8 shows the transient change in birefringence at 650 nm following the same vibrational excitation used above. A prompt drop was observed, directly indicating melting of orbital order. Again, the optically probed state persists for hundreds of picoseconds. The same figure includes a cross

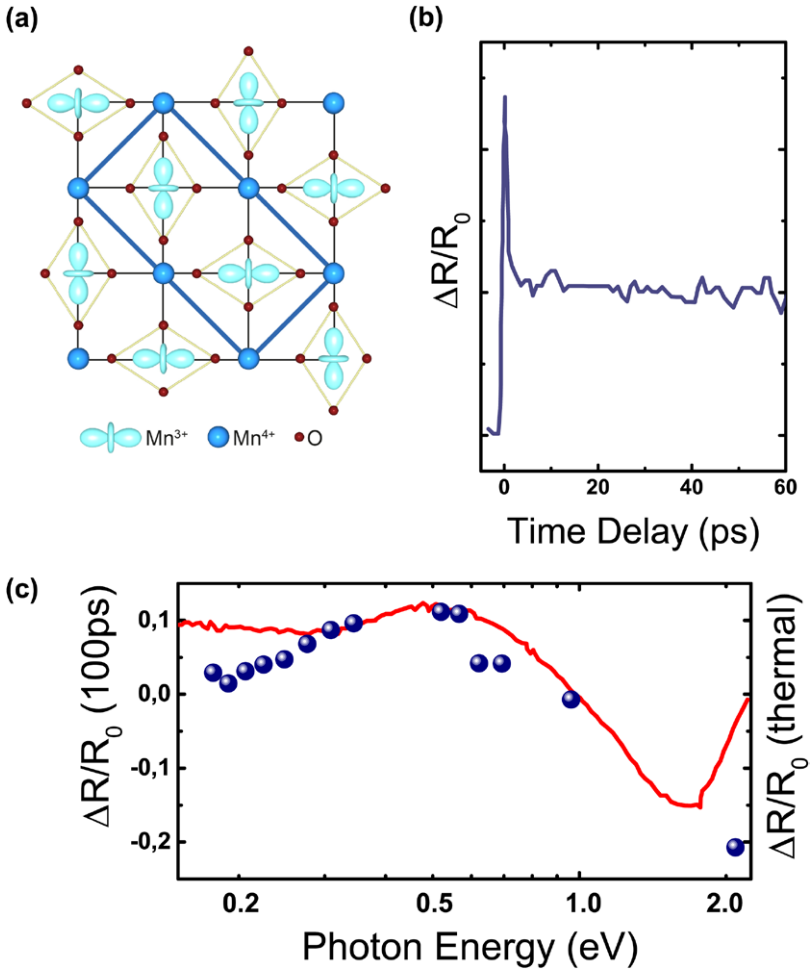

Figure 7. (a) Schematic of charge and orbital order pattern in the *ab*-plane of $La_{0.5}Sr_{1.5}MnO_4$, together with the orbital order unit cell (thick light-blue line). (b) Vibrationally induced changes in reflectivity at 90 K, probed at 650 nm wavelength. (c) The spectrally resolved reflectivity response at 100 ps time delay (blue data points) compared to changes in reflectivity when the sample is heated above the charge ordering temperature (red solid line). Figure adapted from [34, 42].

correlation of the mid-IR pump pulse resonantly driving the Mn–O stretching phonon and the 650 nm probe pulses, as measured by the electro-optic effect in a ZnTe crystal. Birefringence was lost on a timescale identical to the rise time of the excitation pulse, indicative of the ultrafast and non-thermal nature of this process in that it occurs significantly faster than hot optical phonons thermalize in solids [37].

Similar to electric transport and charge/orbital ordering, also magnetism is directly coupled to the lattice in manganites, as observed by the response to external and chemical pressure [23, 38]. However, the optical control of magnetism in solids has for almost two decades been demonstrated with near-infrared excitation only [39–41]. In the experiment by Först *et al* described below, femtosecond mid-infrared pulses were used to excite the same infrared-active Mn–O stretching mode in $La_{0.5}Sr_{1.5}MnO_4$ discussed above and the induced dynamics of spin order was measured by femtosecond resonant soft x-ray diffraction with an x-ray free electron laser [42].

In this experiment, a (1 1 0)-cut $La_{0.5}Sr_{1.5}MnO_4$ single crystal at 25 K lattice temperature was excited by 130 fs, 1.2 mJ cm^{-2} mid-infrared pulses, polarized in the *ab*-plane. These pulses were tuned to a centre wavelength of 13.5 μm (92 meV) with a 4.5 μm FWHM bandwidth, covering the 16 μm (78 meV)

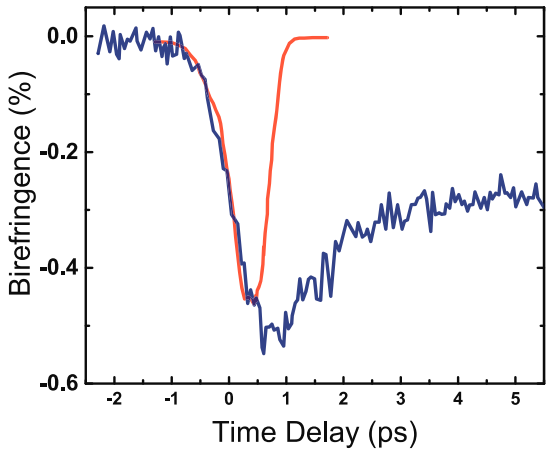

Figure 8. Ultrafast loss of in-plane birefringence in $La_{0.5}Sr_{1.5}MnO_4$ at 650 nm following vibrational excitation (blue solid line). A cross correlation of the mid-infrared pump and the visible probe pulse indicates that melting occurs promptly within the excitation pulse. Figure adapted from [34].

in-plane stretching vibration [29]. The excitation pulses were synchronized to the LCLS x-ray free electron laser (FEL), which was operated at 640 eV photon energy, resonant with

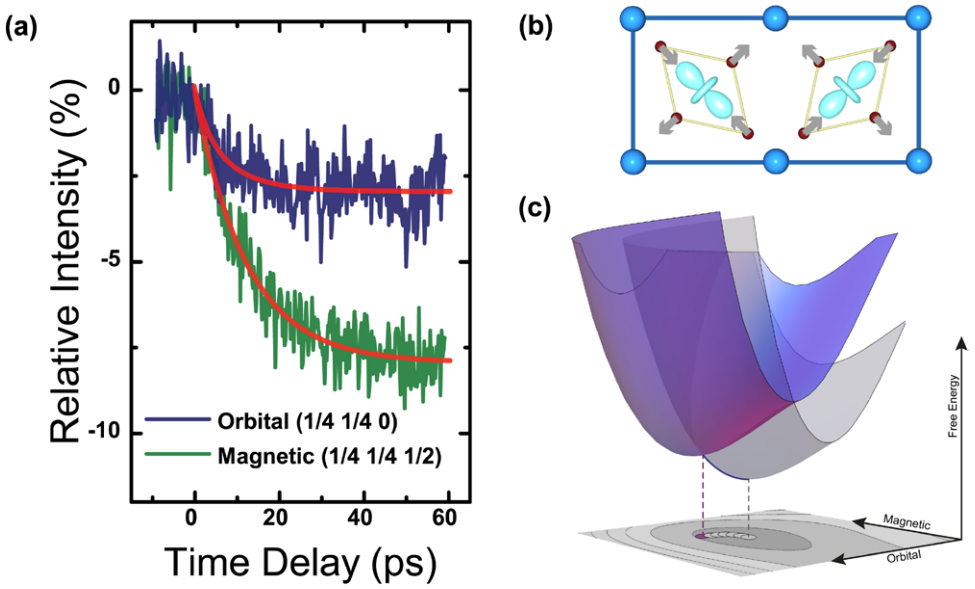

Figure 9. (a) Time-resolved intensity changes of the antiferromagnetic (¼ ¼ ½) and orbital order (¼ ¼ 0) diffraction peaks for vibrational excitation at 13.8 μm wavelength and 1.2 mJ cm^{-2} fluence. The red lines are single exponential fits to the data, with time constants of 6.3 ps and 12.2 ps, respectively. (b) Displacements of Mn and O atoms in the *ab* plane associated with the Raman-active A_g Jahn–Teller mode driven by nonlinear coupling to the optically excited infrared-active in-plane stretching vibration. This mode relaxes the Jahn–Teller distortions to affect the exchange interaction, and thus the electronic and magnetic state of the system, resulting in an effective shift in the equilibrium value of the orbital and magnetic order parameters as illustrated in panel (c). Figure adapted from [42].

the manganese L_3 edge, and spectrally filtered to below 1 eV bandwidth by a grating monochromator. Femtosecond resonant soft x-ray diffraction was then used to probe orbital and magnetic order dynamics with 250 fs time resolution, limited by the timing jitter between the mid-infrared and x-ray pulses.

Figure 9(a) reports the temporal evolution of the integrated diffraction intensity at the antiferromagnetic (¼ ¼ ½) and the charge/orbital order (¼ ¼ 0) peaks. The antiferromagnetic order was reduced by 8% with an exponential decay time of 12.2 ps, while the orbital order dropped by only 3% with a 6.3 ps time constant. We note that this lattice-driven orbital disordering is slower than was observed by time-dependent optical birefringence, with the latter being a less direct method than the resonant x-ray diffraction used here.

Connecting to the discussion of third-order nonlinear phononics above, the in-plane Mn–O stretching mode in $La_{0.5}Sr_{1.5}MnO_4$ excited by the mid-infrared light field has B_{2u} symmetry [43], while the rectified field belongs to the product group $B_{2u} \otimes B_{2u} = A_g$, as is the Raman-active Jahn–Teller mode shown in figure 9(b) [44]. In the equilibrium state, Jahn–Teller distortions lift the degeneracy of the *3d* orbitals to lower the energy of the system, concomitantly stabilizing orbital ordering and affecting exchange interactions to also induce magnetic ordering. Hence the nonlinear phonon coupling could induce relaxation of the Jahn–Teller distortion, in turn decreasing the splitting between crystal field levels and likely reducing the ordering of the orbitals as well as weakening the exchange interactions.

The magnetic and orbital order melting process can be understood along the caricature sketched in figure 9(c). The atomic positions are promptly displaced along the anharmonically coupled Jahn–Teller mode, hence quenching the equilibrium positions of both order parameters to a new value. This displacement of the free energy surface within the magnetic and orbital order parameter plane results in an effective force onto the spin and orbital degrees of freedom driving relaxation toward the bottom of the new free energy surface. The observed timescales for the two order parameters to settle to their new values are significantly different from one another, most likely due to the fact the loss of orbital orientation involves only rearrangements in the E_g electrons and no significant change in spin momentum *per se*. This effect is expected to occur more rapidly. On the other hand, the loss of antiferromagnetic spin order, for which one E_g and three t_{2g} spins rotate, requires a significant exchange of spin angular momentum, and thus has significant inertia.

Again, we note that the ultrafast physical pathway of this lattice-driven insulator-metal control is vastly different from excitation at infrared or visible wavelengths. In that case, the transfer of charges between different on-site orbitals or between adjacent sites triggers the phase transition, subsequently releasing Jahn–Teller distortions and modifying the exchange interactions [45–47].

3. Enhancing superconductivity by nonlinear phononics

We have introduced above how nonlinear lattice dynamics in the doped manganites can melt charge, orbital and magnetic order and turn insulators into metals on the ultrafast time scale. In cuprates, prototypical copper oxide ceramics showing high-temperature superconductivity, the same nonlinear phonon excitation has been used to remove competing charge order and promote superconductivity up to the room temperature scale.

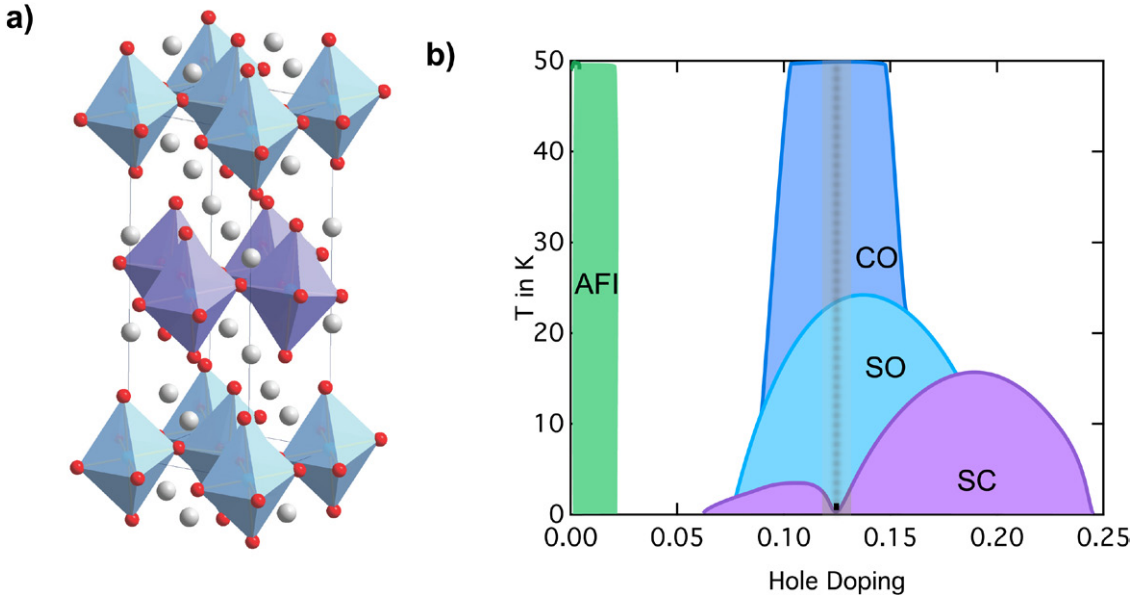

Figure 10. (a) Schematic LTT crystal structure and (b) phase diagram for $La_{1.8-x}Eu_{0.2}Sr_xCuO_4$ ($LESCO_x$). This compound is an antiferromagnetic insulator at zero doping. A low-temperature structural distortion, associated with buckling of the Cu–O planes, quenches superconductivity at all doping levels below 1/8 (vertical dashed line). At this doping, a 1D modulation of charges (CO) and spins (SO), the stripe state, emerges in the planes. At doping levels above 1/8, the compound is superconducting.

3.1. Light-induced superconductivity in single-layer cuprates

La_2CuO_4 is an antiferromagnetic Mott insulator. As holes are doped into the CuO_2 planes by chemical substitution to $La_{2-x}(Ba/Sr)_xCuO_4$, an unconventional metallic phase appears that transforms into a superconductor for $x > 0.05$ and reaches the highest critical temperatures T_C near optimal doping of $x = 0.16$. The $x = 1/8$ compound deserves special attention due to the appearance of a periodic 1D modulation of charges and spins [48, 49] and a concomitant sharp reduction in T_C [50, 51]. In the Ba-doped system, these 'stripes' become static at 1/8-doping, enhanced by periodic buckling of the CuO_2 planes in a low-temperature tetragonal (LTT) phase [52–54].

Static stripes, LTT phases and suppressed superconductivity are also detected in other members of the '214' family of cuprates, such as $La_{1.48}Nd_{0.4}Sr_{0.12}CuO_4$ [49, 55] and $La_{1.675}Eu_{0.2}Sr_{0.125}CuO_4$ ($LESCO_{1/8}$) [56, 57]. Figure 10(a) shows a schematic structure of these compounds depicting CuO_2 layers stacked along the crystallographic c axis. The critical temperature of $LESCO_x$ is strongly reduced for all doping values below and completely suppressed at $x = 1/8$, as illustrated in the phase diagram plotted in figure 10(b) [58, 59].

Understanding the relationship between the superconducting state, stripe order, and the LTT distortion is one of the grand goals in high-T_C superconductivity. It has long been believed that stripes are pinned by the LTT distortion and compete with superconductivity to result in a non-superconducting state. Virtually all studies have explored this interplay by changing static doping or by adiabatically tuning an external parameter. For example, the application of pressure has been shown to restore superconductivity by perturbing the equilibrium crystallographic structure [60, 61].

Fausti *et al* dynamically perturbed the lattice of non-superconducting $LESCO_{1/8}$ by selectively driving an infrared-active lattice vibration with mid-infrared femtosecond pulses [62]. A single-crystal sample, held at a base temperature of 10 K, was excited at 16 μm wavelength (70 meV photon energy), resonant with an in-plane Cu–O stretching mode comparable to that driven in the manganites. Above a threshold fluence of 0.1 mJ cm^{-2}, the 800 nm reflectivity shown in figure 11, which is at least indirectly related to the appearance of superconductivity [63, 64], showed a prompt and long-lived increase following this excitation. In contrast, excitation with out-of-plane

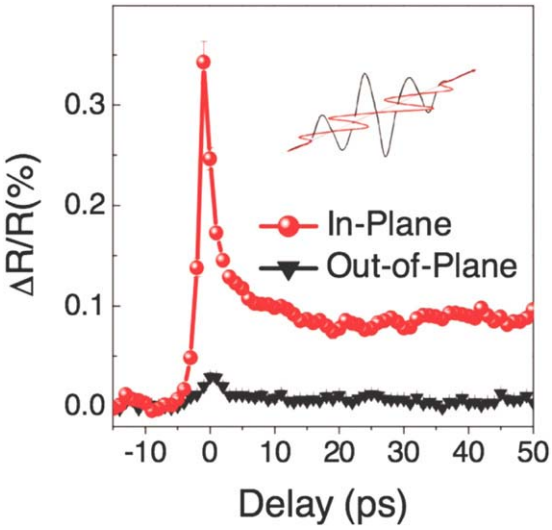

Figure 11. Time dependent reflectivity changes at 800 nm after excitation of $LESCO_{1/8}$ with mid-infrared pulses at 16 μm wavelength and ~1 mJ cm^{-2} intensity. Excitation within the CuO_2 planes results in the appearance of a long-lived (>100 ps) meta-stable phase, while out-of-plane excitation results in minimal reflectivity changes only. Reproduced from [62]. Copyright 2011 with permission from the American Association for the Advancement of Science.

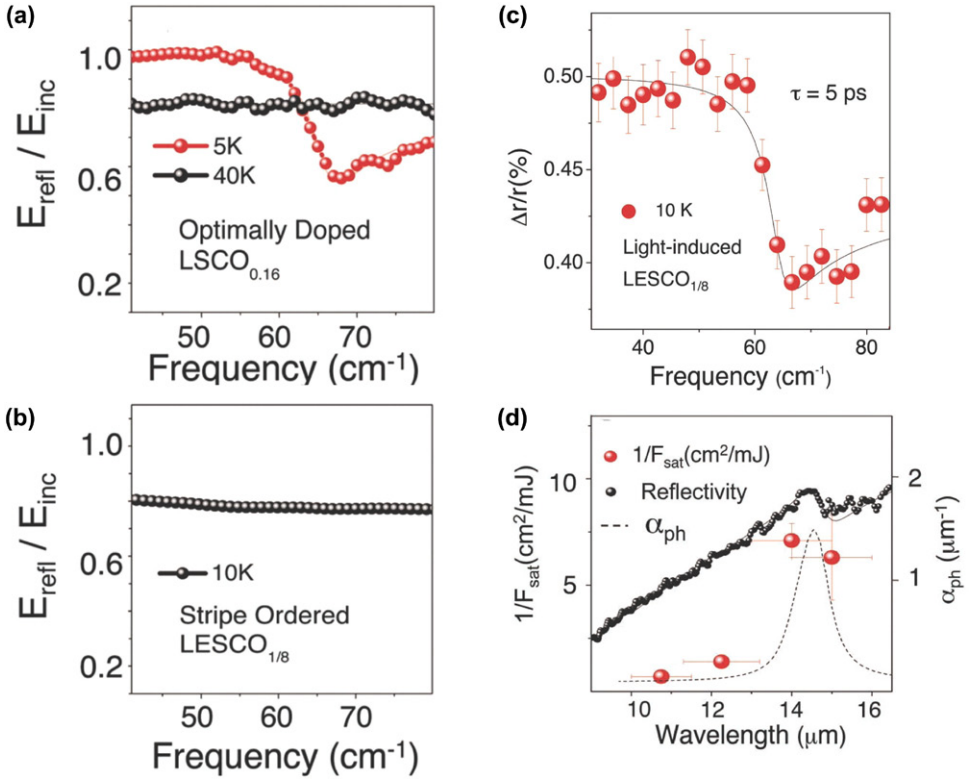

Figure 12. (a) Static *c*-axis electric-field reflectance of $La_{1.84}Sr_{0.16}CuO_4$ ($LSCO_{0.16}$). In the superconducting state at 5 K $< T_C =$ 35 K, the appearance of a Josephson plasma edge reflects the coherent inter-layer transport. Above T_C, incoherent ohmic transport is reflected in a featureless conductivity. (b) Static *c*-axis reflectance of $La_{1.675}Eu_{0.2}Sr_{0.125}CuO_4$ ($LESCO_{1/8}$) at 10 K, showing the optical properties of a non-superconducting compound. (c) Phonon-excitation induced *c*-axis reflectance of ($LESCO_{1/8}$) at 10 K, normalized to the static reflectance, showing a Josephson plasma edge that evidences the photo-induced superconducting-like state. (d) Inverse threshold (photo-susceptibility) as a function of pump wavelength (red dots) compared to the static mid-infrared $LESCO_{1/8}$ reflectivity in the *ab* plane (black dots). The extinction coefficient α (dashed curve) is extracted by means of a Drude–Lorentz fit. Reproduced from [62]. Copyright 2011 with permission from the American Association for the Advancement of Science.

electric field polarization resulted in a small reflectivity change during the pump pulse only, and no long-lived response.

This vibrationally driven state of $LESCO_{1/8}$ was then shown to be superconducting by using time-resolved THz spectroscopy. At equilibrium, superconductivity in the layered cuprates is reflected in the appearance of a Josephson plasma resonance (JPR) in the *c*-axis THz optical properties. This resonance is a general feature observed in layered cuprate superconductors [65], well understood by considering Josephson coupling between stacks of quasi-2D superconducting CuO_2 layers to explain the 3D superconducting state [66–68]. Figure 12(a) reports the static *c*-axis electric-field reflectance of optimally doped $La_{1.84}Sr_{0.16}CuO_4$ below and above the critical temperature $T_C = 35$ K. A plasma edge near 60 cm^{-1} wave numbers emerges in the reflectance of the superconducting state. Above the critical temperature, where interlayer transport is incoherent, the THz spectral response of $La_{1.84}Sr_{0.16}CuO_4$ becomes flat (figure 12(a), black data points). The equilibrium THz electric-field reflectance of non-superconducting $LESCO_{1/8}$ shown in figure 12(b) is also featureless.

Figure 12(c) reports the THz-reflectance in $LESCO_{1/8}$ measured five picoseconds after the mid-infrared resonant excitation of the in-plane Cu–O stretch mode. The clear signature of a plasma edge was found to appear at a frequency comparable to that measured in $LSCO_{0.16}$, evidencing the emergence of photo-induced superconducting-like transport along the *c* axis in $LESCO_{1/8}$. Figure 12(d) plots the pump-wavelength dependence of the inverse fluence threshold for the photo-induced superconductivity in $LESCO_{1/8}$, used as a measure of photo-susceptibility. This data was compared to the wavelength dependent extinction coefficient α near the phonon resonance (dashed line). The observed clear resonance of the photo-susceptibility at the Cu–O stretching mode frequency proved that direct coupling of the light electric field to the crystal structure triggers formation of the superconducting phase.

Further quantitative data analysis required considering a mismatch in penetration depth between the mid-infrared pump (200 nm) and the THz probe pulses (nearly 10 μm), hence assuming a total THz reflectance that results from a homogeneously transformed surface layer and the unperturbed bulk underneath. Here, the knowledge of both amplitude and phase of static and transient field reflectance, as measured through electro-optic sampling, allowed for isolating the real and imaginary part of the time- and frequency-dependent optical conductivity $\sigma_1(\omega,\tau) + i\sigma_2(\omega,\tau)$ in the surface layer. In equilibrium, the low frequency limit $\omega \to 0$ of $\omega\sigma_2(\omega,\tau)$ is proportional to the superfluid density [69]. The same quantity can be dynamically traced by evaluating the low-frequency limit of the measured THz transient electric field at different time delays τ. Figure 13(a) shows the

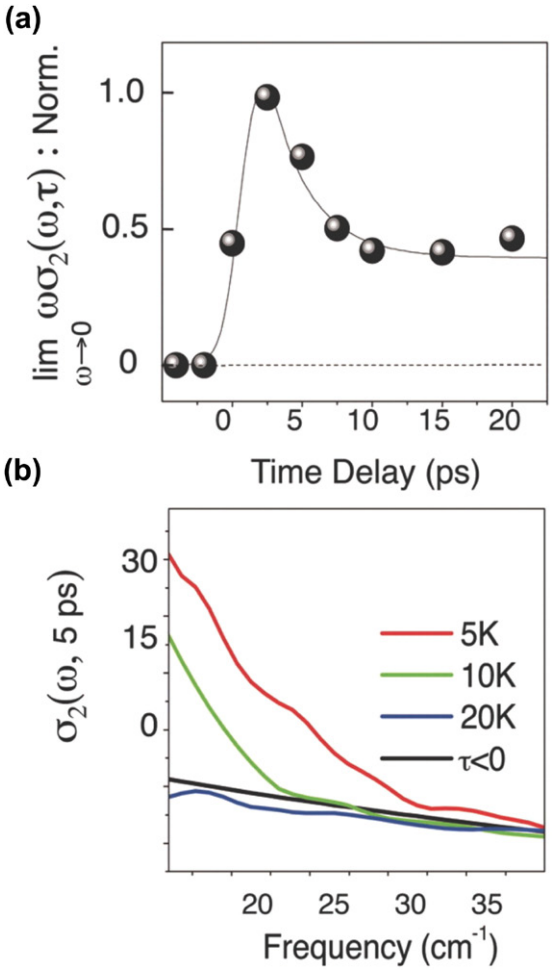

Figure 13. (a) Time dependent plot of the normalized function $\omega\sigma_2(\omega \to 0,\tau)$, proportional to the condensate density, in $LESCO_{1/8}$ at 10 K after excitation with infrared pulses at 16 μm wavelength. The appearance of a $1/\omega$ dispersion demonstrates that the system becomes superconducting. (b) Transient measurement of the imaginary conductivity $\sigma_2(\omega,5\,\text{ps})$, demonstrating that for the fluence used here (<1 mJ cm^{-2}), photo-induced superconductivity can only be induced for base temperatures $T_b < 20$ K. Reproduced from [62]. Copyright 2011 with permission from the American Association for the Advancement of Science.

prompt appearance of finite superconducting density, which was found to relax into a plateau at 5 ps time delay, revealing the formation dynamics of a 3D superconducting-like state. In addition, figure 13(b) shows temperature dependent measurements of $\sigma_2(\omega)$ at $+5$ ps time delays derived after subtraction of a component induced by higher frequency oscillators, which are also perturbed by photo-excitation. The observed divergent imaginary conductivity at low frequencies is another defining characteristic of a superconductor. For the 1 mJ cm^{-2} excitation fluence used in these experiments, the signatures of the transient superconducting-like state were lost above a base temperature of 20 K.

Furthermore, no relaxation of the transient state was found on the measured 100 ps time scale leading to the conclusion that the lifetime of this state exceeds some nanoseconds. The long lifetime was understood such that the broken symmetry of the 3D superconducting state leads to rigidity and to the formation of a kinetic barrier, which stabilizes this state for a long time.

The light-induced Josephson coupling of the CuO_2 planes itself was hypothesized to be the consequence of an instantaneous stripe order melting, mediated by the direct distortion of the lattice through the mid-infrared excitation. The fast time scale of this recoupling was taken as indirect support for the picture of a 2D 'pair-density wave' coherent state [70], in which the charge stripe order suppresses superconductivity only along the *c* axis. Indeed, stripes are compatible with in-plane Cooper pairing in a scenario, where 2D superconducting CuO_2 planes are decoupled due to the periodic charge modulation that prevents interlayer Josephson tunneling [71].

In a second time-resolved experiment, the fate of the charge stripe order and of the LTT distortion during the transition into the transient light-induced 3D superconductor was probed. Först *et al* used femtosecond resonant soft x-ray diffraction in the strongly related stripe-ordered compound $La_{1.875}Ba_{0.125}CuO_4$ to provide insight into the microscopic physics underlying this light-induced state [72]. Both static stripe order and the LTT distortion were measured through resonant diffraction near the oxygen *K*-edge. Here, static charge stripes can be observed at the $q = (0.24\ 0\ 0.5)$ wave vector [58, 73–75], whilst the LTT distortion can be directly measured through the (0 0 1) diffraction peak that is structurally forbidden in the high-temperature phases [75].

These experiments were performed on a $LBCO_{1/8}$ single crystal, held at base temperature $T = 13$ K in the stripe-ordered, LTT-distorted phase. Mid-infrared 200 fs pulses, tuned to the 85 meV (14.5 μm wavelength) resonance of the infrared-active in-plane Cu–O stretching vibration [76], were used for excitation. The pump fluence was kept at 1.9 mJ cm^{-2}, comparable to the conditions of the light-induced superconductivity transition studied in $LESCO_{1/8}$ [62].

The time-dependent integrated scattering intensity of the (0.24 0 0.5) stripe order diffraction peak in response to the mid-infrared excitation is plotted in figure 14(a), showing a prompt decrease by about 70%. The red solid line represents a single-exponential function with a 300 fs time constant, which was used to visualize the prompt reduction of the scattering intensity. These results showed that the mid-infrared pulses melt the stripe order on a subpicosecond timescale, similar to the one observed for the onset of superconductivity in the $LESCO_{1/8}$ THz probe experiments. This implies that the ultrafast formation of the superconducting state and the melting of charge modulations are tightly connected.

In contrast, the evolution of the LTT phase, as probed by the (0 0 1) diffraction peak, was very different from that of the stripe order. The integrated scattered intensity of this structural peak dropped by only 12%, and with a much longer time constant of 15 ps as extracted from a single-exponential fit to the data (red solid line of figure 14(b)). This time constant is likely determined by acoustic propagation when considering that the relaxation of the LTT distortion requires the lattice planes to expand.

These combined experiments demonstrated that the mid-infrared lattice excitation in the striped cuprates triggers the ultrafast formation of a non-equilibrium state, in which stripe charge order has disappeared while the LTT distortion still exists. This decoupling is not present in the equilibrium phase

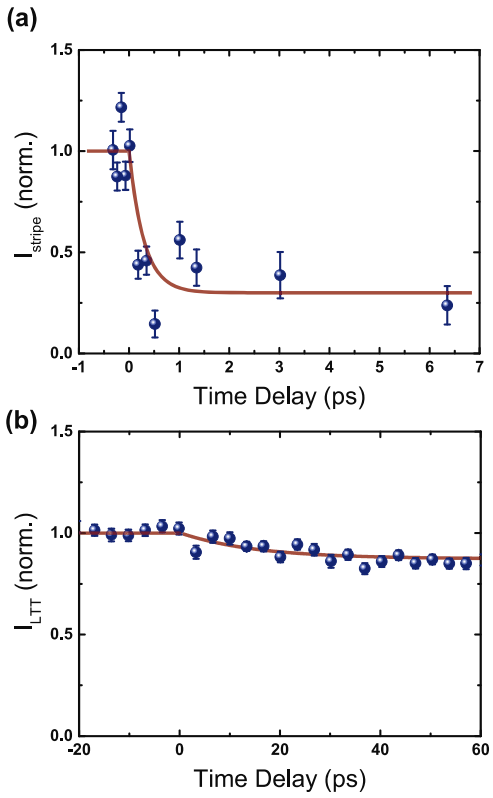

Figure 14. (a) Transient intensity of the charge stripe order diffraction peak in $La_{1.875}Ba_{0.125}CuO_4$ measured at the (0.24 0 0.5) wave vector. Mid-IR excitation, resonant with the in-plance Cu–O stretching mode, at 1.9 mJ cm^{-2} fluence results in a prompt sub-picosecond decrease of the scattered intensity. The red solid line represents an exponential function with a time constant set to 300 fs, i.e. the resolution of the experiment. (b) Light-induced changes in the intensity of the (0 0 1) diffraction peak (reflecting the LTT distortion) in the same $La_{1.875}Ba_{0.125}CuO_4$ crystal under same excitation conditions. The red solid is a single exponential fit to the data yielding a time constant of 15 ps. Figures adapted from [72].

diagram of $LBCO_x$. It was then concluded, that the melting of the charge order by the mid-infrared pulse removes the periodic potential that suppresses interlayer coupling at equilibrium [70, 71]. As result, the 2D superconducting condensates of the CuO_2 planes are free to coherently couple along the *c*-axis and do so on the few-hundred femtosecond time scale of the Josephson plasma resonance. Noteworthy, the LTT distortion plays a minor role in this process, if at all.

The mechanism, by which the excitation of the Cu–O stretching mode melts the charge stripe order, requires further investigation. The combination of microscopic modeling of the lattice anharmonicities with the experimental findings has already proven to be successful for the interpretation of the induced dynamics in manganites. Therefore, future work along these lines could aid understanding the physical pathway of this process, too.

3.2. Light-induced superconductivity and nonlinear lattice dynamics in bi-layer $YBa_2Cu_3O_{6+x}$

Recently, the investigations of light-induced superconductivity were extended to the bilayer high-T_C compound $YBa_2Cu_3O_{6+x}$. Here, similar to the single-layer cuprates discussed above, the superconducting phase at equilibrium involves coherent tunneling between stacks of bilayers that is lost above the transition temperature T_C. Kaiser *et al* demonstrated that resonant lattice excitation enhances this Josephson coupling below T_C and induces coherent interlayer transport at temperatures up to more than 300 K, far above the equilibrium transition temperature [77].

$YBa_2Cu_3O_{6.5}$ ($T_C = 50$ K) crystallizes in an orthorhombic crystal structure and comprises bilayers of CuO_2 planes, separated by an insulating Yttrium layer as shown in figure 15(a). The bilayers are further spaced by Cu–O chains, which control the hole doping of the planes. Similar to the single-layer compounds, the coherent inter-bilayer tunneling in the superconducting state results in the appearance of a JPR in the THz optical properties. This is shown for $YBa_2Cu_3O_{6.6}$ in the upper panel of figure 15(b), where the THz reflectivity is featureless above T_C while a clear edge appears in the superconducting state [78].

The lower panel of figure 15(b) shows the reflectivity changes of $YBa_2Cu_3O_{6.5}$ at 100 K base temperature, i.e. twice the transition temperature of 50 K, at a delay of 0.8 ps after the excitation with 300 fs 15 μm mid-infrared pulses. These light fields were made resonant with the B_{1u} symmetry phonon that involves oscillations of the apical oxygen atoms illustrated in figure 15(a). Following this lattice excitation above T_C, the material was shown to undergo a transition into a non-equilibrium state with striking similarities to the equilibrium superconducting state, evidenced by the appearance of the JPR in the THz reflectivity. This signature of coherent inter-bilayer tunneling was found at temperatures up to 300 K in $YBa_2Cu_3O_{6.5}$ [77].

In addition to this low-frequency JPR at ~50 cm^{-1}, the reflectivity of YBCO features a second edge at higher frequencies—a result of coherence between the neighboring CuO_2 planes within individual bilayers. While inter-bilayer coherence only exists below T_C, signatures of this intra-bilayer coupling have been suggested to persist up to 150 K in $YBa_2Cu_3O_{6.5}$ [79].

In a series of broadband THz probe experiments, Hu *et al* set out to explore the response of both these JPRs to resonant lattice excitation. Strikingly, the appearance of inter-bilayer tunneling has been found to come at the expense of intra-bilayer coupling [80]. A transfer of coherent spectral weight, i.e. spectral weight associated with superconducting charge carriers, from the intra-bilayer to the inter-bilayer junction was observed, which became visible as the appearance of the low-frequency inter-bilayer JPR and a concomitant red-shift of the intra-bilayer JPR. These findings are summarized in figure 16, which shows the frequency-dependent loss function $-\mathrm{Im}(1/\varepsilon)$ in the equilibrium state and in the transient state +0.5 ps after lattice excitation at 100 K.

In search for a microscopic explanation of this highly exotic state, Mankowsky *et al* investigated the underlying nonlinear lattice dynamics in $YBa_2Cu_3O_{6.5}$ using femtosecond hard x-ray diffraction at the LCLS free electron laser [81]. As the direct product $B_{1u} \otimes {}_{1u}$ is of A_g symmetry, the resonantly driven B_{1u} phonon mode of figure 15(a) can only couple to Raman-active phonons of A_g symmetry. Density functional theory (DFT) calculations identified four out of the

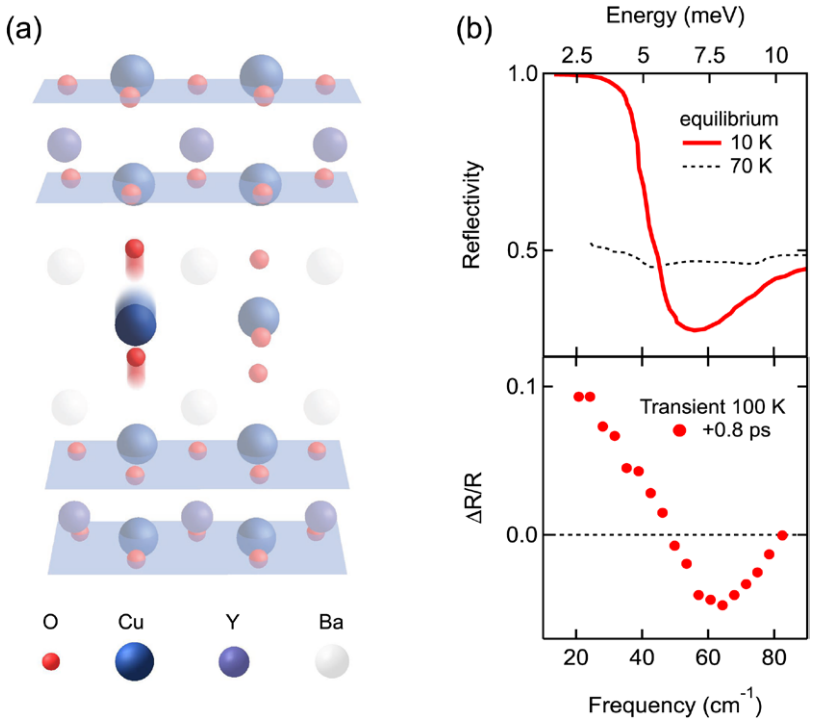

Figure 15. (a) Crystal structure of orthorhombic $YBa_2Cu_3O_{6.5}$ and a sketch of the resonantly excited B_{1u}-symmetry infrared-active phonon mode, comprising c-axis motions of the apical oxygen atoms between bilayers. (b) Upper panel: c-axis static frequency resolved reflectivity of $YBa_2Cu_3O_{6.6}$ above and below the transition temperature of 59 K. Lower panel: light-induced changes in the reflectivity of $YBa_2Cu_3O_{6.5}$ 0.8 ps after excitation (red dots) with 300 fs pulses at 15 μm wavelength, polarized along the c-axis. The base temperature was 100 K. Panel (a) adapted from [81]. Copyright 2014 with permission from Nature Publishing Group. Upper panel (b) adapted from [78]. Copyright 2003 with permission from Elsevier Science Ltd.

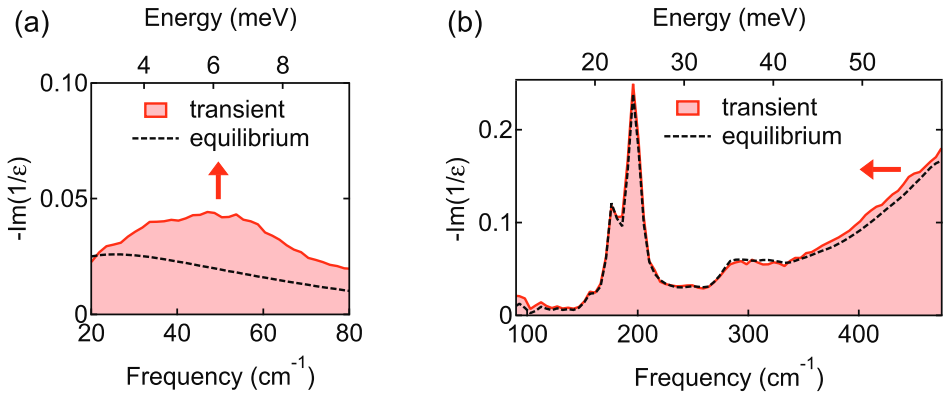

Figure 16. Loss-function of YBCO at 100 K base temperature in the equilibrium (dashed line) and transient state +0.5 ps after excitation. (a) Coherent tunneling induced by resonant lattice excitation appears as a peak in the loss function at low frequencies. The dashed line shows the equilibrium loss-function, which has no frequency-dependent features. (b) This emergence of inter-bilayer coupling is accompanied by a reduction of intra-bilayer coherence, evidenced by a red-shift of the intra-bilayer JPR centered around ~475 cm^{-1}. Adapted from [80]. Copyright 2013 with permission from Nature Publishing Group.

eleven A_g Raman modes—all involving c-axis motions of the apical oxygen and planar copper atoms—to couple strongly. According to the theory of nonlinear phononics, the crystal lattice is then promptly distorted into a non-equilibrium structure along the linear combination of the atomic motions associated with these Raman modes.

Figure 17(a) shows the signature of the nonlinear lattice dynamics following mid-infrared excitation at 4 mJ cm^{-2} fluence and 15 μm wavelength, the same excitation for which light-induced superconductivity was found at 100 K sample temperature. Exemplarily, the (−2 −1 1) and (−2 0 4) diffraction peaks measured with 50 fs x-ray pulses at 6.7 keV photon energy are plotted. A prompt change in diffracted intensity was observed, as expected from the rearrangement of the atoms in the unit cell predicted by the model of nonlinear phonics. The decay to the equilibrium structure happens on the same timescale as the relaxation of the induced coherent interlayer transport measured previously, indicating an intimate connection [77, 80].

The exact amplitude and sign of the changes in diffraction intensity carry significant information on the light-induced

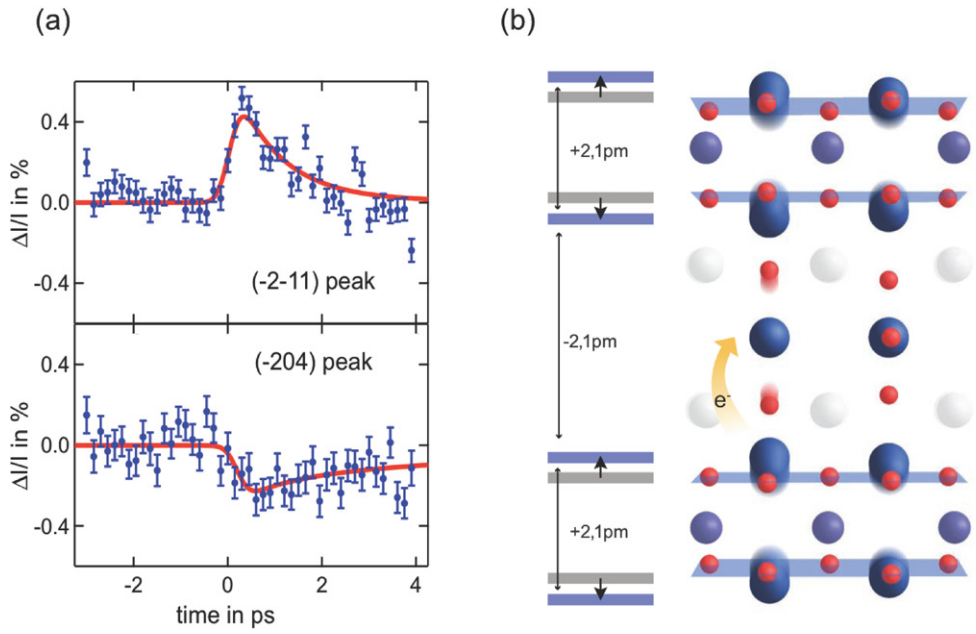

Figure 17. (a) Relative changes in diffracted intensity of the (−2 −1 −1) and the (−2 0 4) Bragg peaks in $YBa_2Cu_3O_{6.5}$, following resonant excitation of the B_{1u}-symmetry mode at 100 K base temperature, i.e. above $T_C = 50$ K. Results of simultaneous fits to all data are shown as solid red lines (see text for details). (b) Sketch of the reconstructed transient crystal structure of $YBa_2Cu_3O_{6.5}$ at the peak signal. The atomic displacements from the equilibrium structure involve a decrease in interbilayer distance, accompanied by an increase in intrabilayer distance. Adapted from [81]. Copyright 2014 with permission from Nature Publishing Group.

lattice rearrangement. In order to reconstruct the transient crystal structure, the computed coupling strengths to the respective A_g Raman modes were combined with structure factor calculations, predicting the changes in diffraction intensity of all 4 measured Bragg peaks for a given B_{1u} amplitude. By using these results and the signal rise and decay times from the THz measurements, all measured Bragg peaks have been fitted simultaneously with only two fitting parameters, that are the amplitude of the resonantly driven infrared-active B_{1u} mode and the relative contribution of the two decay times found in the THz experiment (see [81] for details). The resulting fits are shown as red lines in figure 17(a).

The transient crystal structure, shown in figure 17(b), is composed of an increase in the in-plane O–Cu–O bond buckling and a decrease in apical oxygen—planar copper distance. Furthermore, the intra-bilayer distance increases, whereas the CuO_2 planes within the bilayers move closer together, effectively enhancing the inter-bilayer coupling. This last observation is intuitively consistent with the broadband THz probe measurements, which indicated that the appearance of inter-bilayer coherence comes at the expense of intra-bilayer coupling strength.

DFT calculations using the transient crystal structure further predicted a charge transfer from the CuO_2 planes to the Cu–O chains, effectively increasing the hole doping of the planes. Such self-doping has recently been found to accompany the equilibrium temperature-driven metal-superconductor transition in $YBa_2Cu_3O_{6.9}$ and might be key in explaining the formation of the superconducting phase [82]. Further experiments, for example using time-resolved x-ray absorption spectroscopy, could show whether the charge redistribution predicted here is comparable in magnitude.

Finally, a recent theoretical study by Raines *et al* investigated the effect of the discussed lattice dynamics on the superconductivity and charge order. This work predicted an increase in the transition temperature T_C by up to 100% and a suppression of charge order [83]. The latter was investigated recently in a resonant soft x-ray diffraction study, during which a partial melting of charge order was indeed observed [84], consistent with these theoretical findings.

3.3. Coherent modulation of the $YBa_2Cu_3O_{6.55}$ atomic structure

The lattice dynamics invoked by anharmonic coupling to a resonantly driven infrared-active mode involve two components. First, the crystal lattice experiences a directional displacement along all coupled Raman modes as discussed in the previous section. Secondly the coupled equations (3) and (4) predict that all of the displaced modes, which have a long eigenperiod compared to the excitation pulse duration, will exhibit coherent oscillations about the displaced atomic positions. This section covers measurements of the coherent lattice response using an optical probe, providing a complete picture of the structural dynamics in $YBa_2Cu_3O_{6.55}$ during the light induced metal-superconductor transition [85].

In general, atomic motions along Raman coordinates modulate the polarizability tensor and can be observed as changes in the reflectivity of the material. Therefore, the coherent structural response was measured by probing the transient sample reflectivity using 35 fs pulses at 800 nm wavelength. Mid-infrared pulses of 140 fs duration at 15 μm wavelength were used for excitation of the infrared-active B_{1u} mode. Under these conditions, all A_g symmetry Raman modes with

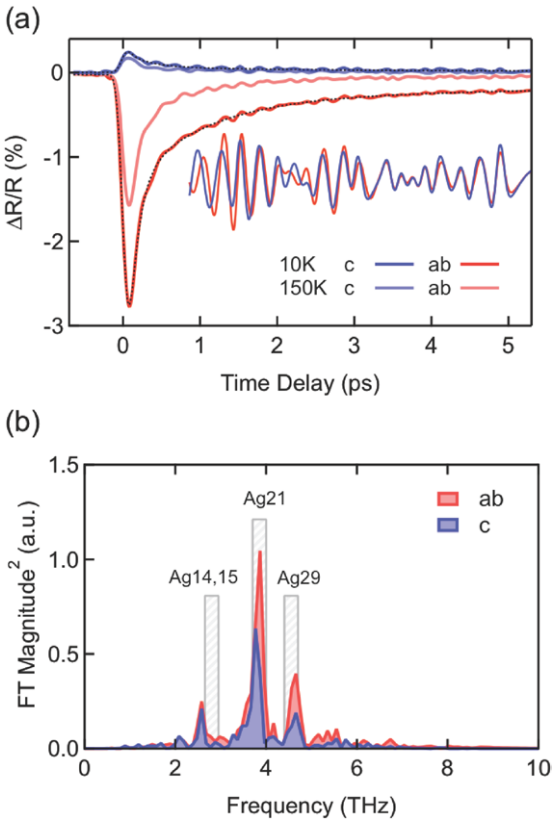

Figure 18. (a) Time-resolved changes in the reflection of 800 nm pulses polarized in-plane *ab* and out-of plane *c* following resonant excitation of the B_{1u} mode in $YBa_2Cu_3O_{6.55}$. The oscillatory components shown in the inset are extracted from the 10 K measurement by subtracting a fit of the background (black line). (b) Fourier transform of these oscillations. The oscillations are composed of three frequency components, which can be attributed to the four Raman modes (Ag14, Ag15, Ag21, Ag29) sorted by ascending frequency. Figures are adapted from [85].

finite coupling to the B_{1u} mode of up to ~6 THz in frequency are expected to be excited in a coherent fashion.

For probe pulse polarizations, both in-plane along the *a* and *b* axes as well as out-of plane along the crystallographic *c* axis, coherent oscillations were found at sample base temperatures below and above T_C. These oscillations are shown in the inset of figure 18(a) for the 10 K measurement, as obtained by subtracting a fit of the background (dashed black line). Three dominant frequency components appeared in the spectrum of the Fourier transform, which were attributed to the four lowest-frequency A_g modes of $YBa_2Cu_3O_{6.55}$ marked in figure 18(b). Consistent with the Raman tensor for the A_g modes, the phase of the coherent response was the same for the two orthogonal probe polarizations [86]. Interestingly, the same coherent oscillations were also found to follow excitation of $YBa_2Cu_3O_{6.9}$ with 2 eV pulses [87–89]. In these studies, however, large changes were found in their amplitudes and relaxation times across the metal-superconductor transition. In contrast, the oscillations reported here continuously increase with decreasing temperature and do not show significant features when crossing T_C. This comparison shows the fundamental difference between conventional stimulated Raman scattering, which involves electronic transitions [6] and its ionic equivalent, which only depends on structural degrees of freedom and is therefore most sensitive to phase transitions that also affect the lattice.

The real-space oscillation amplitudes could not be quantified from the presented data alone, mainly because the changes in the 800 nm polarizability depends on the unknown Raman tensor elements [6]. An estimate of the oscillatory amplitude, however, was obtained by combining these data with the previous x-ray diffraction experiment.

According to this analysis, the atomic motions of the coherently excited modes were dominated by a change in distance of planar Cu atoms *d* along the crystallographic *c* axis, as sketched in figure 19(a). The time-dependent change in this distance is shown in figure 19(b). Following excitation, the Cu atoms of bilayers move apart from each other by ~3 pm, corresponding to a relative change in distance of 1%. This motion is accompanied by coherent oscillations with an estimated amplitude of ~0.9 pm, which decay within 3 ps after excitation.

According to the DFT calculations presented in [81], the oscillatory motions reported above will induce periodic charge redistributions between the Cu atoms of planes and chains, which may cause a dynamical stabilization of interlayer fluctuations by a modulation of electronic properties [90].

4. Vibrational control at complex oxide interfaces

As discussed for the manganites, many of the functional properties of ABO_3 perovskite oxides are extremely sensitive to rotation and tilting of the oxygen octahedra, as these control the hopping amplitudes and the exchange interaction through the B–O–B bond angle and length. Hence, designing or actively controlling such distortions paves the way for engineering the electronic and magnetic properties [91–93].

One class of materials where this approach has been successfully demonstrated is the family rare earth nickelates [94]. At equilibrium, these compounds display a sharp transition from a high-temperature metallic to a low-temperature insulating state [95, 96], which is accompanied by an increase in the Ni–O–Ni bond bending and the appearance of a charge density wave. Additionally, charge disproportionation between adjacent Ni sites is associated with different Ni–O bond lengths [97]. At low temperatures, the nickelates also possess an unusual antiferromagnetic spin arrangement [98]. The transition temperature depends on epitaxial strain, demonstrating sensitivity to lattice distortions [99].

In the following, we show how intense femtosecond mid-infrared pulses can control the electronic properties of a $NdNiO_3$ functional film in a heterostructure—along a non-equilibrium path that involves mechanical coupling to a $LaAlO_3$ substrate, whose Al–O stretching mode is selectively driven by mid-infrared excitation.

In a first set of optical and THz probe experiments [100], Caviglia *et al* used 100 u.c (33 nm) thick $NdNiO_3$ epitaxial thin films deposited on (0 0 1)-oriented $LaAlO_3$ single crystals by off-axis RF magnetron sputtering [101]. This substrate provides –0.5% compressive strain to the material and reduces the metal insulator transition temperature T_{MI} from a bulk value of

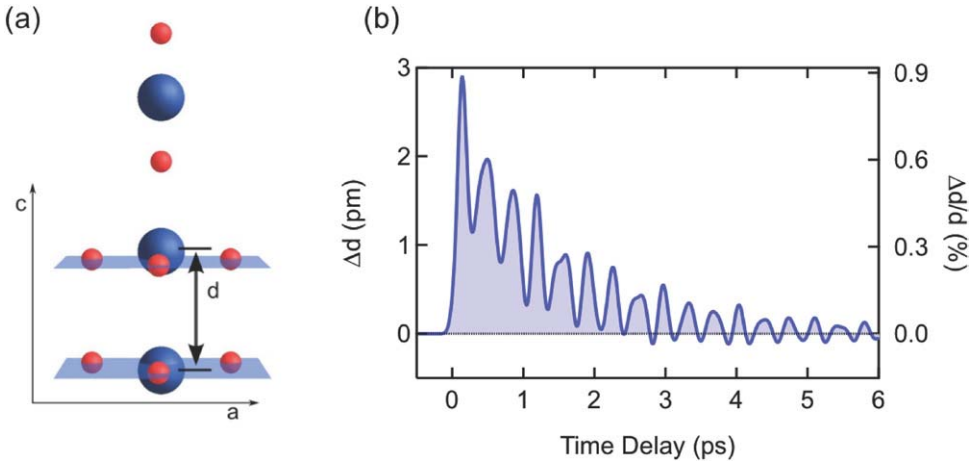

Figure 19. (a) The combined atomic motions of the A_g modes primarily involve c-axis movement of the planar Cu atoms. The distance d between Cu atoms of neighboring CuO_2 planes is defined here to describe the structural dynamics. (b) Changes in this distance d including the full structural dynamics composed of displacive and oscillatory response. Figures are adapted from [85].

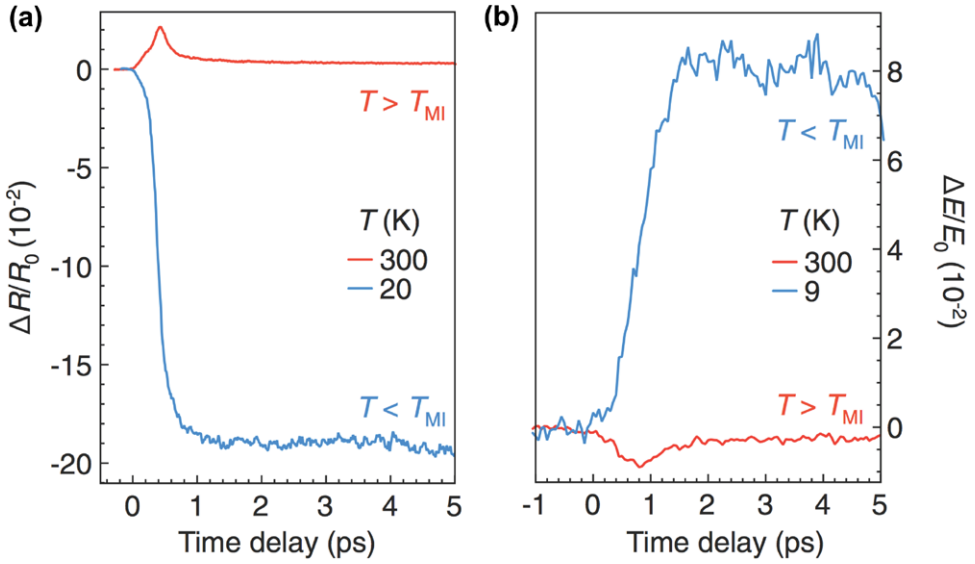

Figure 20. (a) Transient infrared reflectivity changes at 800 nm following vibrational excitation of the $LaAlO_3/NdNiO_3$ heterostructure for two temperatures below and above the insulator-metal transition temperature. (b) Changes of the reflected THz peak electric field showing a long-lived excited state for the same vibrational excitation below T_{MI}. Figures reproduced with permission from [100].

~200 K to about 130 K. 150 fs mid-infrared laser pulses tuned to photon energies between 70 meV and 130 meV (17.7 − 9.5 μm) excited the sample, while transient reflectivity changes in the near-infrared (800 nm, 1.55 eV) and THz (1–6 THz, 5–25 meV) spectral range were used to characterize the electronic properties of $NdNiO_3$ after vibrational excitation.

Figure 20(a) shows the time-resolved near-infrared reflectivity changes induced by 15 μm mid-infrared excitation for different base temperatures. At room temperature, where $NdNiO_3$ is metallic, only a modest and short-lived increase in reflectivity was observed, likely associated to electronic excitations near the Fermi level. Below the metal-insulator transition temperature, however, a hundreds-of-picoseconds long-lived –20% reflectivity change was measured, indicative of the formation of a metastable electronic phase. The time-dependent long-lived increase in the low-frequency THz reflectance (figure 20(b)) suggested that this transient phase was indeed metallic [102]. This interpretation was confirmed by frequency-resolving the THz response for the unperturbed heterostructure and for the photo-induced state, from which a five orders of magnitude increase in DC conductivity was extracted for the $NdNiO_3$ film.

First insight into the driving mechanism for this vibrational control in a heterostructure was gained by analyzing the optical response as function of the pump wavelength. An effective photo-susceptibility for the photo-induced insulator-metal transition was defined from the transient fluence-dependent reflectivity changes whose dependence on the pump photon energy is shown in figure 21 (top panel). Strikingly, this susceptibility was found to follow the absorption of the $LaAlO_3$ substrate vibrational mode rather than that of $NdNiO_3$.

The same dependence was measured in a second sample, a 100 u.c thick $NdNiO_3$ film deposited on a (1 1 0) $NdGaO_3$ single crystal. This substrate provides different mechanical boundary conditions (+1.1% tensile strain), a different phonon frequency and smaller phonon oscillator strength. As for

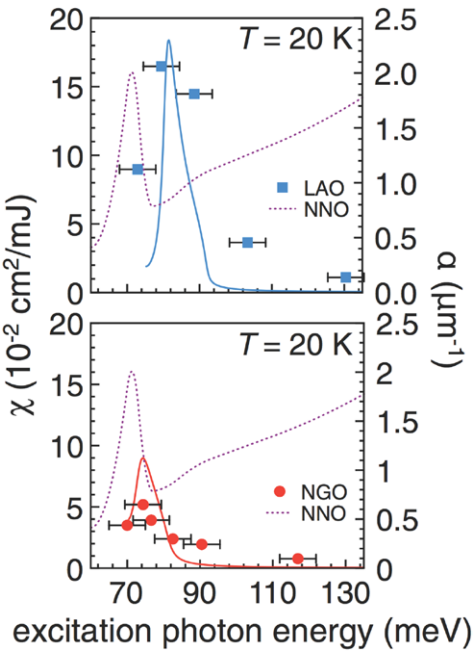

Figure 21. Photo-susceptibility χ of the vibrationally driven insulator-metal transition in $NdNiO_3$ as a function of pump wavelength for the $LaAlO_3$ and $NdGaO_3$ substrate samples. The solid lines show the linear extinction due to the infrared-active phonon of the $LaAlO_3$ (blue) and $NdGaO_3$ (red) crystals [103, 104]. The dashed lines are the linear absorption of bulk $NdNiO_3$ [102]. Figures adapted from [100].

the $LaAlO_3$ substrate, the transient near-infrared reflectivity change below the static metal-insulator transition temperature was negative and long-lived. Also in this heterostructure, the photo-susceptibility peaked at the phonon resonance of the substrate, as shown in figure 21 (bottom). Moreover, the data showed a clear dependence of the amplitude of the photo-susceptibility on the substrate phonon extinction coefficient, which in $LaAlO_3$ is three times larger than for $NdGaO_3$.

These all-optical experiments evidenced that the insulator-metal transition in the functional $NdNiO_3$ film is driven across the interface upon exciting the vibrational mode of the substrate. Time-resolved resonant soft x-ray diffraction was then applied to measure the concomitant magnetic response in the $NdNiO_3$ film with nanometer spatial and femtosecond temporal resolution [105], with the goal of gaining insight into the spatiotemporal dynamics of this ultrafast phase transition. In this experiment, 200 fs pulses tuned to the 15 μm wavelength resonance of the highest-frequency substrate phonon, were used to excite a ~30 nm thick compressively strained $NdNiO_3$ film deposited on a (1 1 1) $LaAlO_3$ crystal. The dynamics of the antiferromagnetic order on the Ni sublattice was measured by detected x-ray pulses tuned to the Ni L_3 edge and diffracted at the corresponding pseudo-cubic (¼ ¼ ¼) wave vector [98].

Figure 22(a) plots the vibrationally induced height changes of this diffraction peak dropping by about 80% within 1.6 ps (blue dots). This time constant was significantly longer than the 250 fs time resolution of the experiment and than the drop time for the case of direct interband excitation homogeneous across the $NdNiO_3$ film [106]. On the other hand, this scale is similar to the time needed for the film to become metallic, as measured by the transient THZ reflectivity in the 1–5 THz range (green dots), suggesting a tight connection between the insulator-to-metal transition and the melting of magnetic order.

Transient θ – 2θ scans for the (¼ ¼ ¼) diffraction peak, which are spatially sensitive to the out-of-plane dynamics of the antiferromagnetic order, are shown in figure 22(b). At negative time delay, homogeneous order across the film with sharp magnetic boundaries was confirmed by the observation of a narrow diffraction peak also exhibiting Laue oscillations. Following the mid-infrared excitation, the reduction in peak height is accompanied by a significant peak broadening and the suppression of the Laue oscillations, implying that the magnetic order melted only over a fraction of the film and that the boundary between the ordered and disordered regions of the film was not sharp.

The spatial distribution of the magnetic order at each time delay was quantitatively analyzed within a model that assumed a soliton-like demagnetization front propagating from the hetero-interface into the thin film, with a smeared and adjustable width of the front that separates the ordered from the disordered region.

Figure 22(c) shows the early time scale evolution of the space-dependent magnetic order, extracted by numerically fitting the diffraction peaks at various time delays using this model. At equilibrium (−0.5 ps), the $NdNiO_3$ film was homogenously ordered across the 30 nm thickness. The analysis further showed that indeed the mid-infrared excitation induced heterogeneous melting, with a demagnetizing phase front that propagates halfway into the film and leaves a magnetically disordered region behind, with a ~10 nm wide boundary between the two regions. Analysis of the time-dependent position of the phase front (not shown here) suggested that the magnetic melt front propagates at a speed of order of, probably even faster than the $NdNiO_3$ longitudinal sound velocity [107].

These experimental results can be explained by considering the direct excitation of the infrared-active phonon mode in the substrate that induces octahedral distortions across the interface to locally act on the electronic and magnetic ordering of the nickelate film. Similar scenarios indeed have been predicted for perovskite heterostructures in the static case [91]. These interfacial structural distortions were proposed to locally create itinerant charge carriers, which are very efficient at scrambling of antiferromagnetic order while diffusing into the $NdNiO_3$ film [108]. The stalling of the phase front halfway across the film could then be ascribed to the transfer of initial kinetic energy into the magnetic sector [109]. This scenario, which was supported by a model Hamiltonian description [105], is also compatible with the similar time scales observed for the insulator-metal transition and the magnetic order melting.

5. Conclusions

We have shown in this review, how intense light fields at mid-infrared wavelengths can be used to drive condensed matter into transient structures that are not achievable at equilibrium. The coupling between different vibrational modes is key to

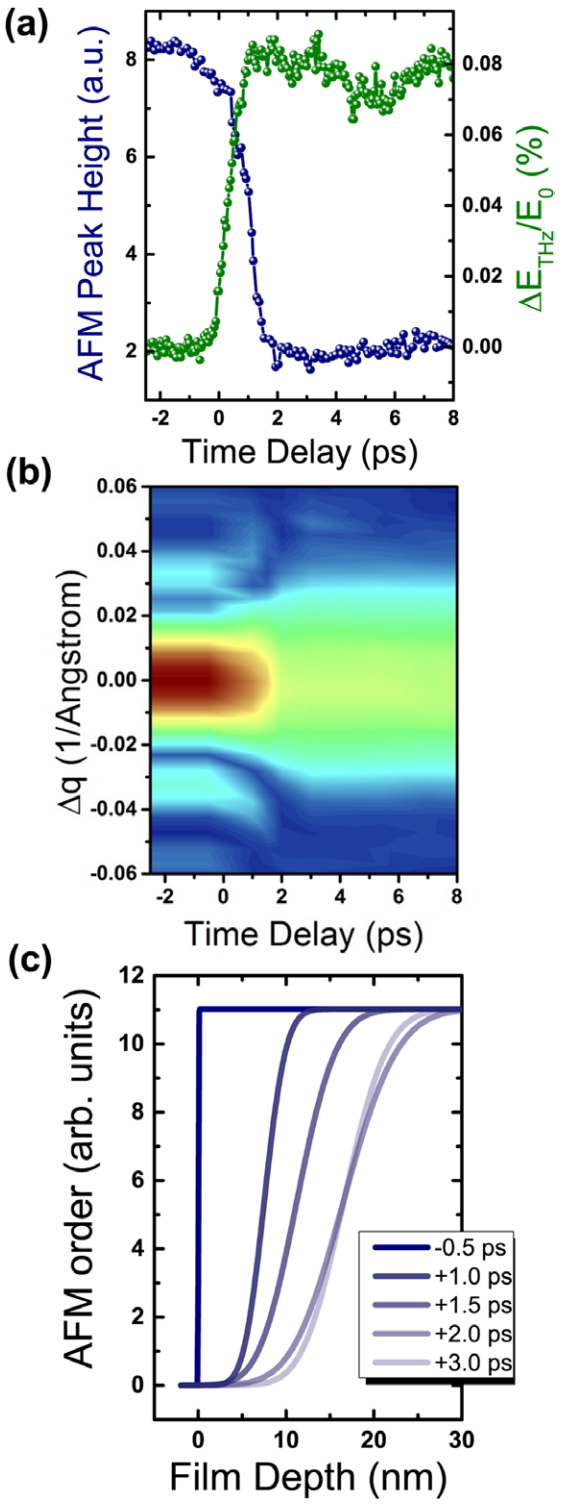

Figure 22. (a) Transient height of the $NdNiO_3$ antiferromagnetic order related (¼ ¼ ¼) diffraction peak at the 852 eV Ni L_3 edge (blue dots) following mid-infrared excitation with a 4 mJ cm^{-2} fluence. The green data points show the transient terahertz reflectivity (see figure 17). The melting of the magnetic order and the insulator–metal transition take place on the same timescale. (b) Short time scale dynamics of the momentum dependence of this diffraction peak, color-coded on a logarithmic scale. (c) Spatiotemporal dynamics of the magnetic order along the [107] sample growth direction, where 0 nm corresponds to the film-substrate interface. These dynamics are extracted from the numerical fits to the data shown in panel (b). Adapted from [105]. Copyright 2015 with permission from Nature Publishing Group.

this effect, which was demonstrated for third-order nonlinearity. In complex oxides, prototypical examples of correlated electron materials, these lattice distortions can lead to electronic and magnetic phase changes, including insulator-metal transitions, rearrangements of spin and orbital order, and even enhanced superconductivity. In the spirit of static materials engineering in complex oxide heterostructures, light-induced deformations of the crystal lattice can also be used to achieve functional control across hetero-interfaces dynamically.

We have summarized the basic theoretical concept of nonlinear phonon interactions and the recent experimental milestones demonstrating the applicability of this mechanism for electronic and magnetic phase control. Optical techniques, such as time-resolved THz spectroscopy are powerful tools to disclose the macroscopic changes along such vibrationally driven phase transitions. On the other hand, ultrafast diffraction in the hard and soft x-ray regime, nowadays possible at free electron lasers, provides knowledge of the non-equilibrium atomic, electronic and magnetic structures that induce these exotic electronic properties. This structural analysis might pave the way for future materials discovery by providing guidelines for the synthesis of condensed matter with improved functionality.

References

[1] Wallis R F and Maradudin A A 1971 Ionic Raman effect II: the first-order ionic Raman effect *Phys. Rev.* B 3 2063
[2] Martin T P and Genzel L 1974 Ionic Raman scattering and ionic frequency mixing *Phys. Status Solidi* b 61 493
[3] Mills D L 1987 Ionic contribution to the Raman tensor of insulators *Phys. Rev.* B 35 9278
[4] Dhar L, Rogers J and Nelson K A 1994 Time-resolved vibrational spectroscopy in the impulsive limit *Chem. Rev.* 94 157
[5] Merlin R 1997 Generating coherent THz phonons with light pulses *Solid State Commun.* 102 207
[6] Stevens T E, Kuhl J and Merlin R 2002 Coherent phonon generation and the two stimulated Raman tensors *Phys. Rev.* B 65 144304
[7] Okimoto Y, Katsufuji T, Ishikawa T, Arima T, Tomioka Y and Tokura Y 1997 Variation of electronic structure in $La_{1-x}Sr_xMnO_3$ ($0 \leqslant x \leqslant 0.3$) as investigated by optical conductivity spectra *Phys. Rev.* B 55 4206
[8] Först M, Manzoni C, Kaiser S, Tomioka Y, Tokura Y, Merlin R and Cavalleri A 2011 Nonlinear phononics as an ultrafast route to lattice control *Nat. Phys.* 7 854
[9] Abrashev M V, Litvinchuk A P, Iliev M N, Meng R L, Popov V N, Ivanov V G, Chalakov R A and Thomsen C 1999 Comparative study of optical phonons in the rhombohedrally distorted perovskites $LaAlO_3$ and $LaMnO_3$ *Phys. Rev.* B 59 4146
[10] Granado E *et al* 1998 Phonon Raman scattering in $R_{1-x}A_xMnO_{3+\delta}$ (R = La, Pr, A = Ca, Sr) *Phys. Rev.* B 58 11435
[11] Först M *et al* 2013 Displacive lattice excitation through nonlinear phononics viewed by femtosecond x-ray diffraction *Solid State Commun.* 169 24
[12] Warren B E 2009 *X-Ray Diffraction* (New York: Dover)
[13] Sokolowski-Tinten K *et al* 2003 Femtosecond x-ray measurement of coherent lattice vibrations near the Lindemann stability limit *Nature* 422 287

[14] Emma P *et al* 2010 First lasing and operation of an ångstrom-wavelength free-electron laser *Nat. Photon.* 4 641

[15] Anderson P W and Hasegawa H 1955 Considerations on double exchange *Phys. Rev.* 100 675

[16] Imada M, Fujimori A and Tokura Y 1998 Metal-insulator transitions *Rev. Mod. Phys.* 70 1039

[17] Goodenough J B 1955 Theory of the role of covalence in the perovskite-type manganites (La, M(II))MnO_3 *Phys. Rev.* 100 564

[18] Tomioka Y, Asamitsu A, Kuwahara H and Moritomo Y 1996 Magnetic-field-induced metal-insulator phenomena in $Pr_{1-x}Ca_xMnO_3$ with controlled charge-ordering instability *Phys. Rev.* B 53 1689

[19] Asamitsu A, Tomioka Y, Kuwahara H and Tokura Y 1997 Current switching of resistive states in magnetoresistive manganites *Nature* 388 50

[20] Kiriukhin V, Casa D, Hill J P, Keimer B, Vigliante A, Tomioka Y and Tokura Y 1997 An x-ray-induced insulator-metal transition in a magnetoresistive manganite *Nature* 386 813

[21] Miyano K, Tanaka T, Tomioka Y and Tokura Y 1997 Photoinduced insulator-to-metal transition in a perovskite manganite *Phys. Rev. Lett.* 78 4257

[22] Fiebig M, Miyano K, Tomioka Y and Tokura Y 1998 Visualization of the local insulator-metal transition in $Pr_{0.7}Ca_{0.3}MnO_3$ *Science* 280 1925

[23] Hwang H Y, Palstra T T M, Cheong S-W and Batlogg B 1995 Pressure effects on the magnetoresistance in doped manganese perovskites *Phys. Rev.* B 52 15046

[24] Rini M, Tobey R, Dean N, Itatani J, Tomiaka Y, Tokura Y, Schoenlein R W and Cavalleri A 2007 Control of the electronic phase of a manganite by mode-selective vibrational excitation *Nature* 449 72

[25] Subedi A, Cavalleri A and Georges A 2014 Theory of nonlinear phononics for coherent light control of solids *Phys. Rev.* B 89 220301

[26] Sternlieb B J, Hill J P, Wildgruber U C, Luke G M, Nachumi B, Moritomo Y and Tokura Y 1996 Charge and magnetic order in $La_{0.5}Sr_{1.5}MnO_4$ *Phys. Rev. Lett.* 76 2169

[27] Senff D, Schumann O, Benomar M, Kriener M, Lorenz T, Sidis Y, Habicht K, Link P and Braden M 2008 Melting of magnetic correlations in charge-orbital ordered $La_{1/2}Sr_{3/2}MnO_4$: competition of ferromagnetic and antiferromagnetic states *Phys. Rev.* B 77 184413

[28] Van den Brink J, Khaliullin G and Khomskii D 1999 Charge and orbital order in half-doped manganites *Phys. Rev. Lett.* 83 5118

[29] Ishikawa T, Ookura K and Tokura Y 1999 Optical response to orbital and charge ordering in a layered manganite: $La_{1/2}Sr_{3/2}MnO_4$ *Phys. Rev.* B 59 8367

[30] Wilkins S B, Spencer P D, Hatton P D, Collins S P, Roper M D, Prabhakaran D and Boothroyd A T 2003 *Phys. Rev. Lett.* 91 167205

[31] Dhesi S S *et al* 2004 Unraveling orbital ordering in $La_{0.5}Sr_{1.5}MnO_4$ *Phys. Rev. Lett.* 92 056403

[32] Wilkins S B, Stojić N, Beale T A W, Binggeli N, Castleton C W M, Bencok P, Prabhakaran D, Boothroyd A T, Hatton P D and Altarelli M 2005 Resonant soft x-ray scattering investigation of orbital and magnetic ordering in $La_{0.5}Sr_{1.5}MnO_4$ *Phys. Rev.* B 71 245102

[33] Staub U, Scagnoli V, Mulders A M, Janousch M, Honda Z and Tonnerre J M 2006 Charge/orbital ordering versus Jahn–Teller distortion in $La_{0.5}Sr_{1.5}MnO_4$ *Europhys. Lett.* 76 926

[34] Tobey R I, Prabhakaran D, Boothroyd A T and Cavalleri A 2008 Ultrafast electronic phase transition in $La_{1/2}Sr_{3/2}MnO_4$ by coherent vibrational excitation: evidence for nonthermal melting of orbital order *Phys. Rev. Lett.* 101 197404

[35] Satpathy S, Popović Z S and Vukajlović F R 1996 *Phys. Rev. Lett.* 76 960

[36] Ogasawara T, Kimura T, Ishikawa T, Kuwata-Gonokami M and Tokura Y 2001 Dynamics of photoinduced melting of charge/orbital order in a layered manganite $La_{0.5}Sr_{1.5}MnO_4$ *Phys. Rev.* B 63 113105

[37] von der Linde D, Kuhl J and Klingenberg H 1980 Raman scattering from nonequilibrium LO phonons with picosecond resolution *Phys. Rev. Lett.* 44 1505

[38] Hwang H Y, Cheong S W, Radaelli P G, Marezio M and Batlogg B 1995 Lattice effects on the magnetoresistance in doped $LaMnO_3$ *Phys. Rev. Lett.* 75 914

[39] Beaurepaire E, Merle J C, Daunois A and Bigot J Y 1999 Ultrafast spin dynamics in ferromagnetic nickel *Phys. Rev. Lett.* 76 4250

[40] Kimel A V, Pisarev R V, Hohlfeld J and Rasing T 2002 Ultrafast quenching of the antiferromagnetic order in $FeBO_3$: direct optical probing of the phonon–magnon coupling *Phys. Rev. Lett.* 89 287401

[41] Stanciu C D, Hansteen F, Kimel A V, Kirilyuk A, Tsukamoto A, Itoh A and Rasing Th 2007 All-optical magnetic recording with circularly polarized light *Phys. Rev. Lett.* 99 047601

[42] Först M *et al* 2011 Driving magnetic order in a manganite by ultrafast lattice excitation *Phys. Rev.* B 84 241104R

[43] Hung J H, Lee H J, Noh T W and Moritomo Y 2000 Infrared phonon study of charge ordering in $La_{1/2}Sr_{3/2}MnO_4$ *J. Phys.: Condens. Matter* 12 9799

[44] Yamamoto K, Kimura T, Ishikawa T, Katsufuji T and Tokura Y 2000 Raman spectroscopy of the charge-orbital ordering in layered manganites *Phys. Rev.* B 61 14706

[45] Beaud P, Johnson S L, Vorobeva E, Staub U, De Souza R A, Milne C J, Jia Q X and Ingold G 2009 Ultrafast structural phase transition driven by photoinduced melting of charge and orbital order *Phys. Rev. Lett.* 103 155702

[46] Ehrke H *et al* 2011 Photoinduced melting of antiferromagnetic order in $La_{0.5}Sr_{1.5}MnO_4$ measured using ultrafast resonant soft x-ray diffraction *Phys. Rev. Lett.* 106 217401

[47] Singla R, Simoncig A, Först M, Prabhakaran D, Cavalieri A L and Cavalleri A 2013 Photoinduced melting of the orbital order in $La_{0.5}Sr_{1.5}MnO_4$ with 4 fs laser pulses *Phys. Rev.* B 88 075107

[48] Zaanen J and Gunnarson O 1989 Charged magnetic domain lines and the magnetism of high-T_C oxides *Phys. Rev.* B 40 7391

[49] Tranquada J, Sternlieb B J, Axe J D, Nakamura Y and Uchida S 1995 Evidence for stripe correlations of spins and holes in copper oxide superconductors *Nature* 375 561

[50] Moodenbaugh A R, Xu Y, Suenaga M, Folkerts T J and Shelton R N 1988 Superconducting properties of $La_{2-x}Ba_xCuO_4$ *Phys. Rev.* B 38 4596

[51] Hücker M, von Zimmermann M, Gu G, Xu Z, Wen J, Xu G, Kang H, Zheludev A and Tranquada J 2011 Stripe order in superconducting $La_{2-x}Ba_xCuO_4$ ($0.095 \leqslant x \leqslant 0.155$) *Phys. Rev.* B 83 104506

[52] Suzuki T and Fujita T 1989 Low-temperature crystalline structure of $(La_{1-x}Ba_x)_2CuO_{4-\delta}$ *Physica* C 159 111

[53] Crawford M K, Harlow R L, McCarron E M, Farneth W E, Axe J D, Chou H and Huang Q 1991 Lattice instabilities and the effect of copper-oxygen-sheet distortions on superconductivity in doped La_2CuO_4 *Phys. Rev.* B 44 7749

[54] Fujita M, Goka H, Yamada K and Matsuda M 2002 Competition between charge- and spin-density-wave order and superconductivity in $La_{1.875}Ba_{0.125-x}Sr_xCuO_4$ *Phys. Rev. Lett.* 88 167008

[55] Nakamura Y and Uchida S 1992 Anisotropic transport properties of single-crystal $La_{2-x-y}Nd_ySr_xCuO_4$: effect of the structural phase transition *Phys. Rev.* B 46 5841

[56] Fink J *et al* 2009 Charge ordering in $La_{1.8-x}Eu_{0.2}Sr_xCuO_4$ studied by resonant soft x-ray diffraction *Phys. Rev.* B 79 100502

[57] Fink J, Soltwisch V, Geck J, Schierle E, Weschke E and Büchner B 2011 Phase diagram of charge order in $La_{1.8-x}Eu_{0.2}Sr_xCuO_4$ from resonant soft x-ray diffraction *Phys. Rev.* B 83 092503

[58] Klauss H-H, Wagener W, Hillberg M, Kopmann W, Walf H, Litterst F J, Hücker M and Büchner B 2000 From antiferromagnetic order to static magnetic stripes: the phase diagram of $(La,Eu)_{2-x}Sr_xCuO_4$ *Phys. Rev. Lett.* 85 4590

[59] Suryadijaya L P, Sasakawa T and Takagi H 2005 Oxygen isotope effect on charge/spin stripes in $La_{1.8-x}Eu_{0.2}Sr_xCuO_4$ *Physica* C 426 402

[60] Takeshita N, Sasagawa T, Sugioka T, Tokura Y and Takagi H 2004 Gigantic anisotropic uniaxial pressure effect on superconductivity within the CuO_2 plane of $La_{1.64}Eu_{0.2}Sr_{0.16}CuO_4$: strain control of stripe criticality *J. Phys. Soc. Japan* 73 1123

[61] Hücker M, von Zimmermann M, Debessai M, Schilling J S, Tranquada J M and Gu G D 2010 Spontaneous symmetry breaking by charge stripes in the high pressure phase of superconducting $La_{1.875}Ba_{0.125}CuO_4$ *Phys. Rev. Lett.* 104 057004

[62] Fausti D, Tobey R I, Dean N, Kaiser S, Dienst A, Hoffmann M C, Pyon S, Takayama T, Takagi H and Cavalleri A 2011 Light induced Superconductivity in a Stripe-ordered cuprate *Science* 331 6014

[63] Segre G P, Gedik N, Orenstein J, Bonn D A, Liang R and Hardy W N 2002 Photoinduced changes of reflectivity in single crystals of $YBa_2Cu_3O_{6.5}$ (Ortho II) *Phys. Rev. Lett.* 88 137001

[64] Giannetti C, Coslovich G, Cilento F, Ferrini G, Eisaki H, Kaneko N, Greven M and Parmigiani F 2009 Discontinuity of the ultrafast electronic response of underdoped superconducting $Bi_2Sr_2CaCu_2O_{8+\delta}$ strongly excited by ultrashort light pulses *Phys. Rev.* B 79 224502

[65] Tamakasu K, Nakamura Y and Uchida S 1992 Charge dynamics across the CuO_2 planes in $La_{2-x}Sr_xCuO_4$ *Phys. Rev. Lett.* 69 1455

[66] Kleiner R, Steinmeyer F, Kunkel G and Müller P 1992 Intrinsic Josephson effects in $Bi_2Sr_2CaCu_2O_8$ single crystals *Phys. Rev. Lett.* 68 2394

[67] Basov D N, Timusk T, Dabrowski B and Jorgensen J D 1994 *C*-axis response of $YBa_2Cu_4O_8$: a pseudogap and possibility of Josephson coupling of CuO_2 planes *Phys. Rev.* B 50 3511

[68] Tajima S, Noda T, Eisaki H and Uchida S 2001 *C*-axis optical response in the static stripe ordered phase of the cuprates *Phys. Rev. Lett.* 86 500

[69] Basov D N, Woods S I, Katz A S, Singley J, Dynes R C, Xu M, Hinks D G, Homes C C and Strongin M 1999 Sum rules and interlayer conductivity of high-T_C cuprates *Science* 283 49

[70] Li Q, Hücker M, Gu G D, Tsvelik A M and Tranquada J 2007 2D superconducting fluctuations in stripe-ordered $La_{1.875}Ba_{0.125}CuO_4$ *Phys. Rev. Lett.* 99 067001

[71] Berg E, Fradkin E, Kim E-A, Kivelson S A, Oganesyan V, Tranquada J M and Zhang S C 2007 Dynamical layer decoupling in a stripe-ordered high-T_C superconductor *Phys. Rev. Lett.* 99 127003

[72] Först M *et al* 2014 Melting of charge stripes in vibrationally driven $La_{1.875}Ba_{0.125}CuO_4$: assessing the respective roles of electronic and lattice order in frustrated superconductors *Phys. Rev. Lett.* 112 157002

[73] Abbamonte P, Rusydi A, Smadici S, Gu G D, Sawatzky G A and Feng D L 2005 Spatially modulated 'Mottness' in $La_{2-x}Ba_xCuO_4$ *Nat. Phys.* 1 155

[74] Wilkins S B *et al* 2011 Comparison of stripe modulations in $La_{1.875}Ba_{0.125}CuO_4$ and $La_{1.48}Nd_{0.4}Sr_{0.12}CuO_4$ *Phys. Rev.* B 84 195101

[75] Dmitrienko V 1983 Forbidden reflections due to anisotropic x-ray susceptibility of crystals *Acta Crystallogr.* A 39 29

[76] Homes C C, Hücker M, Li Q, Xu Z J, Wen J S, Gu G D and Tranquada J M 2012 Determination of the optical properties of $La_{2-x}Ba_xCuO_4$ for several dopings, including the anomalous $x = 1/8$ phase *Phys. Rev.* B 85 134510

[77] Kaiser S *et al* 2014 Optically induced coherent transport far above T_c in underdoped $YBa_2Cu_3O_{6+x}$ *Phys. Rev.* B 89 184516

[78] Timusk T and Homes C C 2003 The role of magnetism in forming the c-axis spectral peak at 400 cm^{-1} in high temperature superconductors *Solid State Commun.* 126 63

[79] Dubroka A *et al* 2011 Evidence of a precursor superconducting phase at temperatures as high as 180 K in $RBa_2Cu_3O_{7-\delta}$ (R = Y, Gd, Eu) superconducting crystals from infrared spectroscopy *Phys. Rev. Lett.* 106 047006

[80] Hu W, Kaiser S, Nicoletti D, Hunt C R, Gierz I, Hoffmann M C, Le Tacon M, Loew T, Keimer B and Cavalleri A 2013 Optically enhanced coherent transport in $YBa_2Cu_3O_{6.5}$ by ultrafast redistribution of interlayer coupling *Nat. Mater* 13 705

[81] Mankowsky R *et al* 2014 Nonlinear lattice dynamics as a basis for enhanced superconductivity in $YBa_2Cu_3O_{6.5}$ *Nature* 516 71

[82] Magnuson M, Schmitt T, Strocov V N, Schlappa J, Kalabukhov A S and Duda L C 2014 Self-doping processes between planes and chains in the metal-to-superconductor transition of $YBa_2Cu_3O_{6.9}$ *Sci. Rep.* 4 7017

[83] Raines Z M, Stanev V and Galitski V M 2015 Enhancement of superconductivity via periodic modulation in a 3D model of cuprates *Phys. Rev.* B 91 184506

[84] Först M *et al* 2014 Femtosecond x rays link melting of charge-density wave correlations and light-enhanced coherent transport in $YBa_2Cu_3O_{6.6}$ *Phys. Rev.* B 90 184514

[85] Mankowsky R, Först M, Loew T, Porras J, Keimer B and Cavalleri A 2015 Coherent modulation of the $YBa_2Cu_3O_{6+x}$ atomic structure by displacive stimulated ionic Raman scattering *Phys. Rev.* B 91 094308

[86] Hayes W and Loudon R 1978 *Scattering of Light by Crystals* (New York: Wiley) ch 1

[87] Albrecht W, Kruse Th and Kurz H 1992 Time-resolved observation of coherent phonons in superconducting $YBa_2Cu_3O_{7-\delta}$ thin films *Phys. Rev. Lett.* 69 1451

[88] Kutt W A, Albrecht W and Kurz H 1992 Generation of coherent phonons in condensed media *IEEE J. Quantum Electron.* 28 2434

[89] Mazin I I, Liechtenstein A I, Jepsen O, Andersen O K and Rodriguez C O 1994 Displacive excitation of coherent phonons in $YBa_2Cu_3O_7$ *Phys. Rev.* B 49 9210

[90] Höppner R, Zhu B, Rexin T, Cavalleri A and Mathey L 2015 Redistribution of phase fluctuations in a periodically driven cuprate superconductor *Phys. Rev.* B 91 104507

[91] He J, Borisevich A, Kalinin S V, Pennycook S J and Pantelidis S T 2010 Control of octahedral tilts and magnetic properties of perovskite oxide heterostructures by substrate symmetry *Phys. Rev. Lett.* 105 227203

[92] May S J, Smith C R, Kim J-W, Karapetrova E, Bhattacharya A and Ryan P J 2012 Control of octahedral rotations in $(LaNiO_3)_n/(SrMnO_3)_m$ superlattices *Phys. Rev.* B 83 153411

[93] Chakhalian J *et al* 2011 Asymmetric orbital-lattice interactions in ultrathin correlated oxide films *Phys. Rev. Lett.* 107 116805

[94] Liu J *et al* 2013 Heterointerface engineered electronic and magnetic phases of $NdNiO_3$ *Nat. Commun.* 4 2714

[95] Medarde M L 1997 Structural, magnetic and electronic properties of $RNiO_3$ perovskites (R = rare earth) *J. Phys.: Condens. Matter* 9 1679

[96] Catalan G 2008 Progress in perovskite nickelate research *Phase Transit.* 81 729

[97] Scagnoli V *et al* 2005 Charge disproportionation and search for orbital ordering in $NdNiO_3$ by use of resonant x-ray diffraction *Phys. Rev.* B 72 155111
[98] Scagnoli V *et al* 2008 Induced noncollinear magnetic order of Nd^{3+} in $NdNiO_3$ observed by resonant soft x-ray diffraction *Phys. Rev.* B 77 115138
[99] Catalan G, Bowman R M and Gregg J M 2000 Metal-insulator transitions in $NdNiO_3$ thin films *Phys. Rev.* B 62 7892
[100] Caviglia A D *et al* 2012 Ultrafast strain engineering in complex oxide heterostructures *Phys. Rev. Lett.* 108 136801
[101] Scherwitzl R *et al* 2010 Electric-field control of the metal-insulator transition in ultrathin $NdNiO_3$ films *Adv. Mater.* 22 5517
[102] Katsufuji T, Okimoto Y, Arima T, Tokura Y and Torrance J B 1995 Optical spectroscopy of the metal-insulator transition in $NdNiO_3$ *Phys. Rev.* B 51 4830
[103] Zhang Z M, Choi B I, Flik M I and Anderson A C 1994 *J. Opt. Soc. Am.* B 11 2252
[104] Nuzhnyy D, Petzelt J, Kamba S, Martí X, Čechal T, Brooks C M and Schlom D G 2011 *J. Phys.: Condens. Matter* 23 045901
[105] Först M *et al* 2015 Spatially resolved ultrafast magnetic dynamics launched at a complex-oxide hetero-interface *Nat. Mater.* 14 883
[106] Caviglia A D *et al* 2013 Photoinduced melting of magnetic order in the correlated electron insulator $NdNiO_3$ *Phys. Rev.* B 88 220401
[107] Ruello P, Zhang S, Laffez P, Perrin B and Gusev V 2009 Laser-induced coherent acoustical phonons mechanisms in the metal-insulator transition compound $NdNiO_3$: thermal and nonthermal processes *Phys. Rev.* B 79 094303
[108] Brinkman W F and Rice T M 1979 Single-particle excitations in magnetic insulators *Phys. Rev.* B 2 1324
[109] Buleavskii L N, Nagaev E L and Khomskii D I 1968 A new type of auto-localized state of a conduction electron in an antiferromagnetic semiconductor *Sov. Phys.– JETP* 27 836